Check for updates

21699402, 2020, 10, Downloaded from https://agupubs.onlinelibrary.wiley.com/doi/10.1029/2020JA028393 by Test, Wiley Online Library on [04/01/2023]. See the Terms and Conditions (https://onlinelibrary.wiley.com/terms-and-conditions) on Wiley Online Library for rules of use; OA articles are governed by the applicable Creative Commons License

AGU ADVANCING EARTH AND SPACE SCIENCE

JGR Space Physics

RESEARCH ARTICLE
10.1029/2020JA028393

Key Points:
- Nonlinear dispersive fast magnetosonic waves produce 2-D compressible turbulence downstream of the termination shock
- Taylor's hypothesis breaks down in the subfast magnetosonic solar wind in the inner heliosheath
- The magnetic turbulence spectrum observed by Voyager 2 in the inner heliosheath is reproduced by self-consistent three-fluid MHD simulation

Correspondence to:
B. Zieger,
berci@bu.edu

Citation:
Zieger, B., Opher, M., Tóth, G., & Florinski, V. (2020). Dispersive fast magnetosonic waves and shock-driven compressible turbulence in the inner heliosheath. *Journal of Geophysical Research: Space Physics*, *125*, e2020JA028393. https://doi.org/10.1029/2020JA028393

Received 23 JUN 2020
Accepted 15 SEP 2020
Accepted article online 24 SEP 2020

©2020. American Geophysical Union. All Rights Reserved.

Dispersive Fast Magnetosonic Waves and Shock-Driven Compressible Turbulence in the Inner Heliosheath

Bertalan Zieger[1], Merav Opher[1,2], Gábor Tóth[3], and Vladimir Florinski[4]

[1]Center for Space Physics, Boston University, Boston, MA, USA, [2]Astronomy Department, Boston University, Boston, MA, USA, [3]Department of Climate and Space Sciences and Engineering, University of Michigan, Ann Arbor, MI, USA, [4]Department of Space Science, University of Alabama, Huntsville, AL, USA

Abstract The solar wind in the inner heliosheath beyond the termination shock (TS) is a nonequilibrium collisionless plasma consisting of thermal solar wind ions, suprathermal pickup ions, and electrons. In such multi-ion plasma, two fast magnetosonic wave modes exist, the low-frequency fast mode and the high-frequency fast mode. Both fast modes are dispersive on fluid and ion scales, which results in nonlinear dispersive shock waves. We present high-resolution three-fluid simulations of the TS and the inner heliosheath up to a few astronomical units (AU) downstream of the TS. We show that downstream propagating nonlinear fast magnetosonic waves grow until they steepen into shocklets, overturn, and start to propagate backward in the frame of the downstream propagating wave. The counterpropagating nonlinear waves result in 2-D fast magnetosonic turbulence, which is driven by the ion-ion hybrid resonance instability. Energy is transferred from small scales to large scales in the inverse cascade range, and enstrophy is transferred from large scales to small scales in the direct cascade range. We validate our three-fluid simulations with in situ high-resolution Voyager 2 magnetic field observations in the inner heliosheath. Our simulations reproduce the observed magnetic turbulence spectrum with a spectral slope of −5/3 in frequency domain. However, the fluid-scale turbulence spectrum is not a Kolmogorov spectrum in wave number domain because Taylor's hypothesis breaks down in the inner heliosheath. The magnetic structure functions of the simulated and observed turbulence follow the Kolmogorov-Kraichnan scaling, which implies self-similarity.

1. Introduction

Multi-ion plasma, in general, contains more than one ion species (e.g., H^+ and He^{++}) or multiple ion populations with distinct physical characteristics, for example, two ion populations with different bulk velocities (ion beams) or with different temperatures (nonequilibrium plasmas). The latter is common in magnetized collisionless space plasmas that include an ion source due to the ionization of a moving ambient neutral gas component. A typical example is the solar wind in the outer heliosphere, where a cold thermal ion population coexists with a hot suprathermal pickup ion (PUI) population. PUIs are created through charge exchange between solar wind protons and the neutral hydrogen component of the local interstellar medium and accelerated by the convection electric field of the solar wind. Other examples include the interaction region of the supersonic solar wind with cometary atmospheres, exospheres of weakly magnetized planets (Mars and Pluto), and the neutral hydrogen geocorona of Earth or the interaction of planetary magnetospheric plasma with neutral sources from their moons (Io and Titan). It has remained largely unexplored how magnetosonic waves propagate and form shocks in such plasmas.

The Voyager spacecraft are the first man-made objects to cross the TS (termination shock Stone et al., 2005, 2008), where the solar wind becomes subfast magnetosonic due to the interaction with the local interstellar medium. Voyager 2 observations revealed that classical single-fluid magnetohydrodynamic (MHD) or multispecies single-fluid MHD models (Isenberg, 1986, Usmanov & Goldstein, 2006, Usmanov et al., 2014, Whang, 1998, Zank et al., 2010, Zieger et al., 2013; where the ion species and electrons are comoving) are not sufficient to describe the observed nonlinear waves downstream the TS. Consequently, more sophisticated physical models, like multifluid MHD, hybrid or fully kinetic solar wind models, are needed to capture nonlinear waves, dispersive shock waves, and ion-ion instabilities, where each ion species (and electrons) can move independently with their own velocities, and the fluctuating parts of the ion velocities are often comparable to the mean velocity of the collective plasma fluid.

21699402, 2020, 10, Downloaded from https://agupubs.onlinelibrary.wiley.com/doi/10.1029/2020JA028393 by Test, Wiley Online Library on [04/01/2023]. See the Terms and Conditions (https://onlinelibrary.wiley.com/terms-and-conditions) on Wiley Online Library for rules of use; OA articles are governed by the applicable Creative Commons License

One important aspect to note is that by the very nature of PUIs (as they are picked up by the solar wind), they have the same average velocity as the thermal component: $\widetilde{\mathbf{u}}_{PUI} = \widetilde{\mathbf{u}}_{SW}$. However, the fluctuating parts ($\mathbf{u}''_{PUI}$ and $\mathbf{u}''_{SW}$) responsible for waves and turbulence can be different and quite large as nonlinear structures develop, where the ion velocities are decomposed to an average part and a fluctuating part as $\mathbf{u}_{PUI} = \widetilde{\mathbf{u}}_{PUI} + \mathbf{u}''_{PUI}$ and $\mathbf{u}_{SW} = \widetilde{\mathbf{u}}_{SW} + \mathbf{u}''_{SW}$. It is therefore necessary to solve the full multifluid equations with different momentum and energy equations for each ion species, unlike in multispecies single-fluid models, where only one momentum equation is solved for the collective fluid.

In multifluid MHD models of the solar wind (Opher et al., 2020; Zank et al., 2014; Zieger et al., 2015), suprathermal PUIs, thermal solar wind ions, and electrons are treated as three separate fluids with different ion velocities. Our multifluid MHD model was successful in reconstructing the nonlinear structure of the Voyager 2 TS crossing (Zieger et al., 2015). The addition of hot suprathermal ions to the mixture of thermal solar wind protons and electrons results in a high-frequency fast (HFF) mode and a low-frequency fast (LFF) mode, both of which are dispersive on fluid and ion scales. Positive dispersive wave modes can produce positive dispersive shock waves with a precursor wave train, and negative dispersive wave modes can produce negative dispersive shock waves with a trailing wave train (Biskamp, 1973; Hoefer, 2014). Dispersion is positive if the group velocity $\frac{\mathrm{d}\omega}{\mathrm{d}k}$ increases with increasing wave number, that is, $\frac{\mathrm{d}^2\omega}{\mathrm{d}k^2} > 0$, and it is negative if the group velocity decreases with increasing wave number, that is, $\frac{\mathrm{d}^2\omega}{\mathrm{d}k^2} < 0$. It was shown that the TS is a high-β low-Mach number (1.56) subcritical shock with a trailing wave train (Zieger et al., 2015), which is a negative dispersive shock wave in the LFF mode. Subcritical fast magnetosonic shocks are defined with the criterium $u_{n,2} < c_{s,2}$; that is, the normal component of the downstream flow velocity is smaller than the downstream sound speed (Coroniti, 1970).

In case of subcritical high-β perpendicular shocks (where the fast Mach number is less than 2.76), kinetic effects such as ion reflection, shock surfing, and shock reformation can be neglected and the shock structure is controlled by dispersion (Balogh & Treumann, 2013; Edmiston & Kennel, 1984), which justifies the multifluid approach. However, in the high-β regime, the shock criticality strongly depends on the obliquity of the shock with the critical Mach number approaching one for parallel shocks. Using the properties of the trailing wave train downstream the TS, Zieger et al. (2015) were able to constrain the previously unknown PUI abundance and temperature. Their multifluid MHD simulations also confirmed the presence of a hot electron population at the TS, which has been predicted by a number of previous theoretical studies (Chalov & Fahr, 2013; Chashei & Fahr, 2014; Fahr et al., 2014). They showed that a significant part of the upstream kinetic energy of solar wind ions is transferred to the heating of PUIs and massless electrons, while the total hydrodynamic energy is conserved across the shock. A multifluid MHD model provides self-consistent energy partitioning across the TS, unlike the multispecies single-fluid models where additional assumptions are needed about the behavior of PUIs (Zank et al., 2010). In this paper, we present high-resolution three-fluid simulations of the TS and the inner heliosheath up to a few AU downstream of the TS. The three-fluid model produces self-consistent compressible turbulence in the inner heliosheath even with constant solar wind conditions upstream of the TS. We discuss the spectral properties and the spatial/temporal evolution of the turbulence and compare our results with in situ Voyager 2 observations in the inner heliosheath.

The paper is structured as follows. In section 2, we briefly review the theory of dispersive magnetosonic waves and dispersive shock waves in collisionless plasma. In section 3, we present our multifluid numerical simulation of compressible turbulence downstream of the TS and compare the simulation with the theoretical predictions. In section 4, we validate the simulation results with in situ Voyager 2 observations in the inner heliosheath. Conclusions are presented in section 5.

2. Theory of Dispersive Fast Magnetosonic Waves in Nonequilibrium Collisionless Plasma

2.1. Dispersion Relation

The solar wind in the inner heliosheath beyond the TS is a nonequilibrium collisionless plasma consisting of thermal solar wind ions, suprathermal PUIs, and electrons. Since the thermalization time scale is much larger than the convection time scale, and the convection time scale is much larger than the isotropization time scale of PUIs, the three-fluid description of the inner heliosheath plasma is a reasonable approximation.

21699402, 2020, 10, Downloaded from https://agupubs.onlinelibrary.wiley.com/doi/10.1029/2020JA028393 by Test, Wiley Online Library on [04/01/2023]. See the Terms and Conditions (https://onlinelibrary.wiley.com/terms-and-conditions) on Wiley Online Library for rules of use; OA articles are governed by the applicable Creative Commons License

We use the standard set of multi-ion multifluid Hall MHD equations (Glocer et al., 2009; Zieger et al., 2015) to describe the three-fluid solar wind model with thermal solar wind ions (SW), PUIs, and electrons:

$$\frac{\partial \rho_j}{\partial t} + \nabla \cdot (\rho_j \mathbf{u}_j) = 0, \tag{1}$$

$$\frac{\partial (\rho_j \mathbf{u}_j)}{\partial t} + \nabla \cdot (\rho_j \mathbf{u}_j \mathbf{u}_j + p_j \tilde{\mathbf{I}}) = n_j q_j (\mathbf{u}_j - \mathbf{u}_+) \times \mathbf{B} + \frac{n_j q_j}{n_e e} (\mathbf{J} \times \mathbf{B} - \nabla p_e), \tag{2}$$

$$\frac{\partial \epsilon_j}{\partial t} + \nabla \cdot \left[(\epsilon_j + p_j) \mathbf{u}_j \right] = \mathbf{u}_j \cdot \left[n_j q_j (\mathbf{u}_j - \mathbf{u}_+) \times \mathbf{B} + \frac{n_j q_j}{n_e e} (\mathbf{J} \times \mathbf{B} - \nabla p_e) \right], \tag{3}$$

$$\frac{\partial \mathbf{B}}{\partial t} + \nabla \times (-\mathbf{u}_e \times \mathbf{B}) = 0, \tag{4}$$

$$\frac{\partial p_e}{\partial t} + \nabla \cdot (p_e \mathbf{u}_e) = -(\gamma - 1) p_e \nabla \cdot \mathbf{u}_e, \tag{5}$$

where ρ, n, q, $\mathbf{u}$, and p are mass density, number density, electric charge, velocity, and thermal pressure, respectively; index j stands for the two ion fluids (SW and PUI), and subscript e stands for the electron fluid; $\mathbf{B}$ is the magnetic field vector; $\mathbf{J} = \nabla \times \mathbf{B}/\mu_0$ is the current density; μ_0 is the permeability of free space; e is the elementary charge; $\gamma = 5/3$ is the adiabatic index; ϵ_j is the energy density of ion fluid j, defined as

$$\epsilon_j = \frac{\rho_j \mathbf{u}_j \mathbf{u}_j}{2} + \frac{p_j}{\gamma - 1}; \tag{6}$$

$\mathbf{u}_+$ is the charge averaged ion velocity, defined as

$$\mathbf{u}_+ = \frac{\sum_j n_j q_j \mathbf{u}_j}{\sum_j n_j q_j}, \tag{7}$$

and the electron velocity including the Hall term is

$$\mathbf{u}_e = -\frac{\mathbf{J}}{n_e e} + \mathbf{u}_+. \tag{8}$$

We solve separate continuity, momentum, and energy equations for each ion fluid and close the set of multifluid MHD equations with the electron pressure equation. Heat conduction and viscosity is neglected in the collisionless solar wind plasma. Because of the relatively small characteristic length scale of our simulation (2 AU), we also neglect charge exchange, which plays otherwise an important role in global models of the inner heliosheath (Fahr et al., 2016; Opher et al., 2020; Scherer et al., 2018).

Linearizing the continuity and momentum Equations 1 and 2, we can derive the following general dispersion relation of perpendicular magnetosonic waves in warm multifluid plasma (for the detailed derivation see Appendix B in Zieger et al., 2015):

$$\left(\sum_j \frac{\omega_{pj}^2 \Omega_j}{\omega^2 - c_j^2 k^2 - \Omega_j^2} \right)^2 - \left(c^2 k^2 + \sum_j \frac{\omega_{pj}^2 (\omega^2 - c_j^2 k^2)}{\omega^2 - c_j^2 k^2 - \Omega_j^2} \right) \left(\sum_j \frac{\omega_{pj}^2}{\omega^2 - c_j^2 k^2 - \Omega_j^2} \right) = 0, \tag{9}$$

where ω and k are the wave frequency and wave number, respectively; ω_{pj}, Ω_j, and c_j are the plasma frequency, the gyrofrequency, and the sound speed of particle species j; and c is the speed of light. In case of three fluids, that is, thermal solar wind ions, PUIs, and electrons, Equation 9 reduces to a second-order polynomial equation in ω^2, which can be solved analytically (Toida & Aota, 2013; Zieger et al., 2015).

There are two linear plane wave solutions: a LFF mode and a HFF mode. Thus, the multi-ion nature of the plasma creates two kinds of fast magnetosonic waves: a low-frequency mode that propagates mainly in the cold thermal population and a high-frequency mode that propagates mainly in the hot PUI population.

The HFF mode has a cutoff frequency ($\omega_{PUI\,0}$) at the small wave number limit ($k \to 0$) that is independent of the plasma β defined as $\beta = 2\mu_0(p_{SW} + p_{PUI} + p_e)/B^2$:

$$\omega_{PUI0} = \left(\frac{\omega_{pSW}^2}{\Omega_{SW}^2} + \frac{\omega_{pPUI}^2}{\Omega_{PUI}^2} \right) \frac{\Omega_{SW}\Omega_{PUI}|\Omega_e|}{\omega_{pe}}. \tag{10}$$

The resonance frequency of the LFF mode is the ion-ion hybrid resonance frequency defined as

$$\omega_{SWr} = \left(\frac{\omega_{pSW}^2\Omega_{PUI}^2 + \omega_{pPUI}^2\Omega_{SW}^2}{\omega_{pSW}^2 + \omega_{pPUI}^2} \right)^{1/2}, \tag{11}$$

whereas the resonance frequency of the HFF mode is the lower-hybrid frequency defined as

$$\omega_{PUIr} = \left(\frac{\Omega_e^2}{\omega_{pe}^2}(\omega_{pSW}^2 + \omega_{pPUI}^2) \right)^{1/2}. \tag{12}$$

If both the solar wind ions and the PUIs are protons, Equation 10 reduces to $\omega_{PUI0} = \Omega_H$, where Ω_H is the proton gyrofrequency, Equation 11 reduces to $\omega_{SWr} = \Omega_H$, and Equation 12 reduces to $\omega_{PUIr} = (\Omega_H\Omega_e)^{1/2}$.

In the cold plasma limit ($\beta = 0$), LFF waves in a two-ion species plasma (e.g., H^+ and He^{++}) propagate in the frequency range between zero and the ion-ion hybrid resonance frequency, whereas HFF waves propagate in the frequency range between the cutoff frequency of the HFF mode and the lower hybrid frequency. There is a small frequency gap between the ion-ion hybrid resonance frequency and the cutoff frequency of the HFF mode, where linear magnetosonic waves cannot propagate. We are going to show that this is not true in the inner heliosheath, where the cold plasma approximation breaks down because β is of the order of 10 (McComas et al., 2017; Randol et al., 2013; Zieger et al., 2015).

In order to study the propagation of fast magnetosonic waves in the inner heliosheath on a theoretical basis, we calculated the multifluid linear dispersion relation, phase velocity, and group velocity of perpendicular fast magnetosonic waves downstream of the TS, which are shown in Figure 1. Here the frequency is normalized to the proton gyrofrequency Ω_H, and the wave number is normalized to the reciprocal of the electron inertial length ω_{pe}/c. We used the downstream solar wind parameters for the third TS crossing (TS3) of Voyager 2 ($u_{SW,2}$ = 181.6 km/s, $n_{SW,2}$ = 0.002375 cm^{-3}, $T_{SW,2}$ = 0.2532 MK, B_2 = 0.1247 nT, $n_{PUI,2}$ = 0.0005943 cm^{-3}, $T_{PUI,2}$ = 20.34 MK, $p_{e,2}$ = 0.05638 pPa). These parameters are the mean downstream solutions of the best fitting three-fluid model of the TS3 crossing in the hot electron case (Zieger et al., 2015). Similar mean downstream solutions were obtained for the extended shock simulation presented in section 3.

As shown in Figure 1a, the HFF mode has a cutoff frequency at the proton gyrofrequency (Ω_H), while the LFF mode can propagate at low frequencies without any frequency cutoff. The cutoff frequency of the HFF mode and the resonance frequencies of the LFF and HFF modes are marked with dashed lines in Figure 1a. Note that the resonance frequency of the LFF mode ($\omega_{SWr} = \Omega_H$) coincides with the cutoff frequency of the HFF mode ($\omega_{PUI0} = \Omega_H$), and there is no frequency gap between the two. This implies that the HFF mode becomes unstable at the long wavelength (i.e., small wave number) limit ($k \to 0$) due to the ion-ion hybrid resonance instability of thermal solar wind ions and PUIs. The ion-ion hybrid resonance is expected to heat the solar wind plasma in the inner heliosheath. Unlike in case of cold plasma ($\beta = 0$), the frequencies of the LFF and the HFF waves do not approach the ion-ion resonance frequency and the lower hybrid frequency, respectively, at high wave numbers, but continue to increase with k above these resonance frequencies. Thus, the LFF and HFF modes become unstable at the wave number where their dispersion relation crosses the corresponding resonance frequency. The resonance points of the LFF and HFF modes are marked with blue and red asterisk symbols, respectively, in Figure 1a. These resonance points predict narrow spectral peaks at the corresponding wave numbers in the turbulence spectra of the solar wind in the inner heliosheath. The ion-ion hybrid resonance instability in the LFF mode is predicted at the wave number of 0.00726 ω_{pe} (see blue asterisk in Figure 1a).

In reality, the solar wind contains not only protons but also He^{++} ions (α particles) and other heavy ion species of very small abundance, and the PUIs are not purely interstellar H^+ (protons) but contain interstellar He^+ as well. Thus, multifluid theory predicts multiple narrow spectral peaks in the observed turbulence spectrum in the inner heliosheath, at the wave numbers of the ion-ion hybrid resonance instability of the H^+, He^{++}, and He^+ fast magnetosonic modes.

21699402, 2020, 10, Downloaded from https://agupubs.onlinelibrary.wiley.com/doi/10.1029/2020JA028393 by Test, Wiley Online Library on [04/01/2023]. See the Terms and Conditions (https://onlinelibrary.wiley.com/terms-and-conditions) on Wiley Online Library for rules of use; OA articles are governed by the applicable Creative Commons License

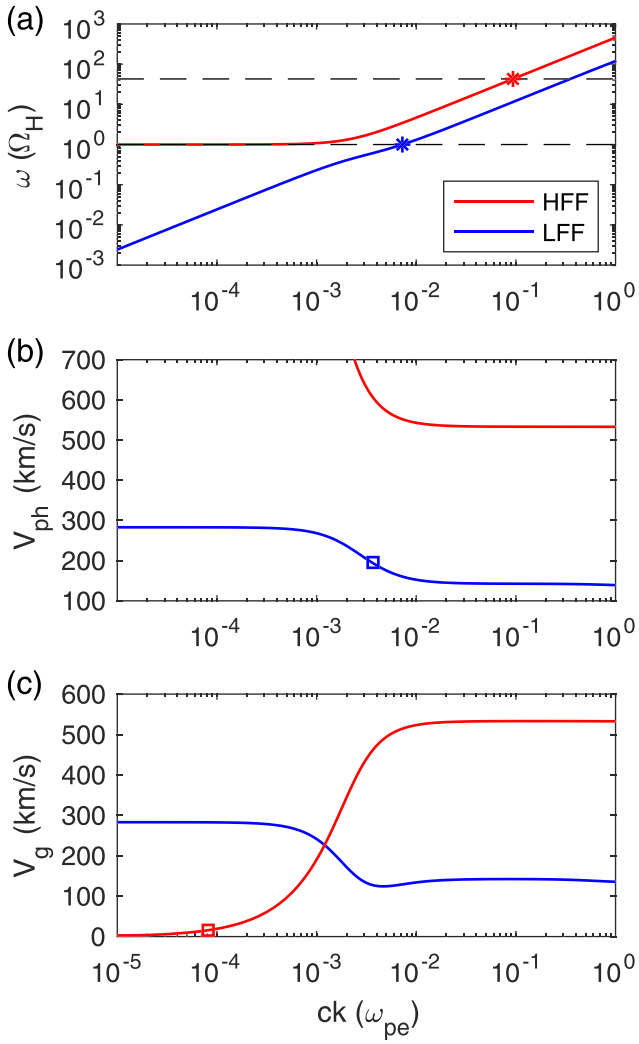

Figure 1. Characteristics of perpendicular fast magnetosonic waves downstream of the TS. (a) Dispersion relations of the high-frequency fast mode (HFF) or pickup ion mode and of the low-frequency fast mode (LFF) or solar wind ion mode. The cutoff frequency of the HFF mode and the resonance frequencies of the LFF and HFF modes are shown as dashed lines. The resonance points of the LFF and HFF modes are marked with asterisk symbols. (b) Phase velocities of the HFF mode and of the LFF mode. The blue square symbol marks the phase velocity and wave number of the quasi-stationary waves shown in Figure 2b. (c) Group velocities of the HFF mode and of the LFF mode. The red square symbol marks the propagation velocity and wave number of the magnetic holes shown in Figure 2c. The HFF mode is positive dispersive, and the LFF mode is negative dispersive on fluid scales. The wave number is normalized to the reciprocal of the electron inertial length.

2.2. Dispersive Shock Waves and Shocklets

In single-ion plasma, magnetosonic waves become dispersive on the scale of the Debye length. However, in nonequilibrium plasma, like the solar wind that consists of thermal solar wind ions and hot PUIs, both fast magnetosonic wave modes are dispersive on ion scales and even on fluid scales. The HFF mode is positive dispersive because its group velocity increases with increasing wave number (see Figure 1c). On the other hand, the LFF mode is negative dispersive on fluid scales because its group velocity is decreasing with increasing wave number. On ion scales, however, the LFF mode becomes positive dispersive at higher wave numbers (between 0.005 and 0.05 ω_{pe}), as shown in Figure 1c.

Biskamp (1973) was among the first to suggest on the basis of theoretical considerations that subcritical shocks can produce a quasi-stationary trailing wave train downstream of the shock or a quasi-stationary precursor wave train upstream of the shock depending on the shape of the dispersion relation. If a linear dispersion relation bends upward (the group velocity increases) or downward (the group velocity decreases)

21699402, 2020, 10, Downloaded from https://agupubs.onlinelibrary.wiley.com/doi/10.1029/2020JA028393 by Test, Wiley Online Library on [04/01/2023]. See the Terms and Conditions (https://onlinelibrary.wiley.com/terms-and-conditions) on Wiley Online Library for rules of use; OA articles are governed by the applicable Creative Commons License

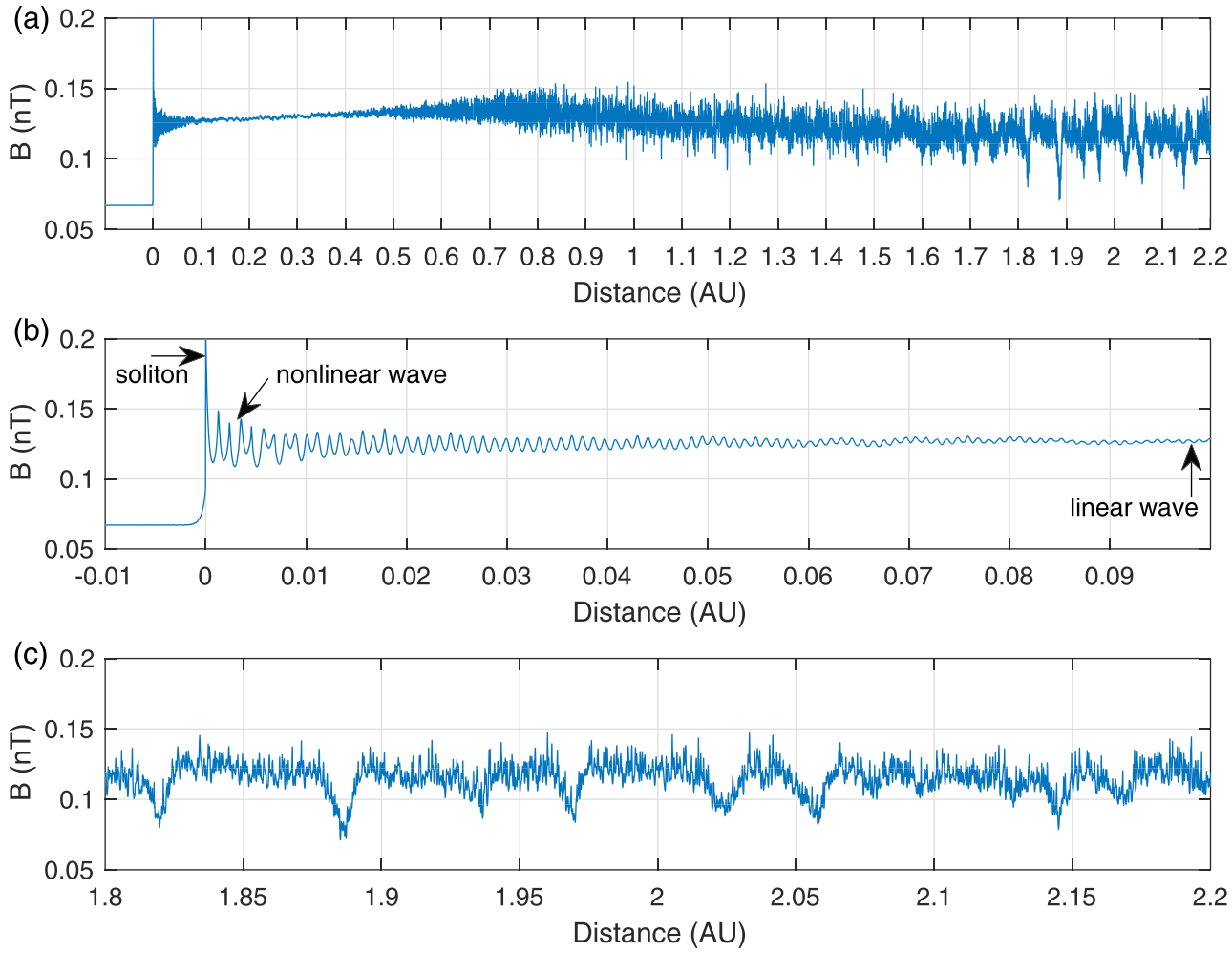

Figure 2. Three-fluid simulation of the TS and the turbulent inner heliosheath. (a) Magnetic field variations at and beyond the TS up to 2.2 AU downstream. (b) High-resolution section at the TS showing a coherent quasi-stationary dispersive shock wave with a soliton edge, a linear wave edge, and oscillatory nonlinear waves between the two (indicated by arrows). (c) High-resolution section in the inner heliosheath showing fully developed compressible turbulence with large-scale magnetic field depressions (magnetic holes).

at higher wave numbers, it will result in a precursor or trailing wave train, respectively. Thus, a subcritical shock in the negative dispersive LFF mode is expected to produce a trailing wave train, which has been confirmed by our numerical three-fluid simulation of the TS (see Figure 2b). More recently, Hoefer (2014) studied the long-term behavior of weak (small jump in density) dispersive shock wave solutions for dispersive Eulerian fluids without viscosity and heat conduction. It was shown that negative dispersive shock waves have a nonlinear trailing wave train downstream of the shock and positive dispersive shock waves have a nonlinear precursor wave train upstream of the shock. The dispersive shock wave has a stationary soliton edge (overshoot) at the shock front where the wave number approaches zero ($k \rightarrow 0$) and a linear wave edge downstream or upstream of the shock front, where the amplitude approaches zero. Interestingly, the velocity of the soliton edge is not the same as the velocity of the linear wave edge, which results in an expanding dispersive shock wave both in the negative and positive dispersion cases. In dispersive Eulerian fluids with zero viscosity and zero thermal conductivity, like a two-temperature collisionless plasma, weak shocks are characterized by an expanding oscillatory region with two speeds, in contrast to localized shock fronts propagating as travelling waves in classical, viscous fluids.

The overturning of downstream propagating compressional waves in collisionless dispersive plasma has been predicted by theory (Biskamp, 1973; McKenzie et al., 1993). For sufficiently small amplitudes, plane

21699402, 2020, 10, Downloaded from https://agupubs.onlinelibrary.wiley.com/doi/10.1029/2020JA028393 by Test, Wiley Online Library on [04/01/2023]. See the Terms and Conditions (https://onlinelibrary.wiley.com/terms-and-conditions) on Wiley Online Library for rules of use; OA articles are governed by the applicable Creative Commons License

21699402, 2020, 10, Downloaded from https://agupubs.onlinelibrary.wiley.com/doi/10.1029/2020JA028393 by Test, Wiley Online Library on [04/01/2023]. See the Terms and Conditions (https://onlinelibrary.wiley.com/terms-and-conditions) on Wiley Online Library for rules of use; OA articles are governed by the applicable Creative Commons License

waves in a dispersive system can be described by the nonlinear Korteweg de Vries equation:

$$\frac{\partial u}{\partial t} + (u \pm c_s)\frac{\partial u}{\partial x} = a\frac{\partial^3 u}{\partial x^3}, \tag{13}$$

where u is the velocity amplitude, c_s is the sound speed, and the right-hand side term is the dispersion term, where a is the dispersion parameter. At the weak dispersion limit, the right-hand side becomes negligible. First, we consider an upstream propagating wave with a negative sign in Equation 13. The wave becomes stationary ($\partial/\partial t = 0$) if $u = c_s$, which defines the sonic point. Now, we consider an upstream propagating wave with a positive sign in Equation 13. Applying Galilean transformation to Equation 13, we move to the frame that propagates with the sound speed in the downstream direction and find that the velocity is conserved ($\mathrm{d}u/\mathrm{d}t = 0$) at the weak dispersion limit ($a \to 0$). This means that a faster fluid element can overtake a slower fluid element ($\partial u/\partial x \to \infty$). The nonlinear steepening leads to a shocklet and eventually to the overturning of the wave. The solutions of the nonlinear Korteweg de Vries equation (Equation 13) for an upstream propagating disturbance are either periodic nonlinear waves or symmetric solitary waves (solitons). However, the soliton is transformed to an oscillatory shock wave if a small amount of dissipation is added (Biskamp, 1973).

In multi-ion plasma, the generalized sonic point is reached when the upstream propagating magnetosonic wave becomes stationary: $\partial u_j/\partial t = 0$. On the other hand, the critical locus is reached when the downstream propagating magnetosonic wave steepens into a shocklet and overturns in the frame propagating at the sound speed of the respective ion fluid (SW or PUI): $\mathrm{d}u_j/\mathrm{d}x \to \infty$. In multi-ion magnetized plasma, the generalized sonic point and the critical locus do not coincide (Dubinin et al., 2006). Thus, the nonlinear steepening of downstream propagating fast magnetosonic waves predicts both solar wind ion shocklets and PUI shocklets in the inner heliosheath that appear as thin current sheets or sudden jumps in the magnetic field intensity. The overturning of nonlinear fast magnetosonic waves results in counterpropagating waves, which is expected to drive strong compressible turbulence in the inner heliosheath even under steady upstream solar wind conditions.

2.3. Compressible Turbulence

Since the solar wind bulk flow velocity is mostly perpendicular to the ambient magnetic field in the inner heliosheath where Voyager 2 crossed the TS and the velocity perturbations of perpendicular fast magnetosonic waves are in the plane perpendicular to the ambient magnetic field, the magnetosonic turbulence in the inner heliosheath is expected to be 2-D compressible turbulence with no or negligible velocity perturbations in the parallel direction. What makes the difference between incompressible and compressible turbulence? The governing equations of incompressible turbulence are the conservation of mass, momentum, and magnetic flux, and the unknown variables are the velocity and magnetic field vectors and the plasma pressure. In the case of compressible turbulence, we have an additional equation for the conservation of energy and the equation of state, and there are two more unknown variables, the density and the energy.

In incompressible flows, we can decompose any variable Φ into a mean part ($\overline{\Phi}$) and a fluctuating part (Φ') using Reynolds averaging of the governing equations: $\Phi = \overline{\Phi} + \Phi'$, where $\overline{\Phi}$ is the average of Φ over time. The turbulent kinetic energy density is then defined as $\overline{u_i' u_i'}/2$, where u_i is the ith velocity component. However, this is not applicable in compressible flows because the density is not constant. In highly compressible flows, Favre averaging is needed to decompose some of the turbulent variable to $\Phi = \tilde{\Phi} + \Phi''$, where $\tilde{\Phi}$ is the density weighted average of Φ over time, that is, $\tilde{\Phi} = \overline{\rho\Phi}/\bar{\rho}$. In the compressible case, the turbulent kinetic energy density is defined as $\widetilde{u_i'' u_i''}/2$, that is, $\overline{\rho u_i'' u_i''}/(2\bar{\rho})$ and the mean kinetic energy density is $\tilde{u}_i\tilde{u}_i/2$. In the averaged equations of compressible turbulence, Reynolds decomposition is used for the density, pressure, and magnetic field, and Favre decomposition is used for the velocity and the energy. Accordingly, we used Favre decomposition when calculating the turbulent kinetic energy spectra of solar wind ions and PUIs in Figure 4. However, the difference between the Reynolds and Favre averaged mean ion velocities in the inner heliosheath is typically less than 1%, which is negligible. Thus, it would be sufficient to decompose all variables, including velocity and energy, with Reynolds averaging.

21699402, 2020, 10, Downloaded from https://agupubs.onlinelibrary.wiley.com/doi/10.1029/2020JA028393 by Test, Wiley Online Library on [04/01/2023]. See the Terms and Conditions (https://onlinelibrary.wiley.com/terms-and-conditions) on Wiley Online Library for rules of use; OA articles are governed by the applicable Creative Commons License

In incompressible 2-D plasma turbulence, the enstrophy is defined as the surface integral of the square of the vorticity

$$Z(\mathbf{u}) = \frac{1}{2}\int_S |\nabla \times \mathbf{u}|^2 \mathrm{d}S. \tag{14}$$

In simple terms, it is related to the energy associated with the eddy motion of the plasma, and as such, it is conservative like the kinetic energy

$$E(\mathbf{u}) = \frac{1}{2}\int_S |\mathbf{u}|^2 \mathrm{d}S, \tag{15}$$

as shown in turbulence theory (Kraichnan, 1967). More generally, when we are not restricted to incompressible flow, the enstrophy can be defined as the surface integral of the square of the Frobenius norm of the velocity gradient

$$Z(\mathbf{u}) = \frac{1}{2}\int_S ||\nabla \mathbf{u}||^2 \mathrm{d}S. \tag{16}$$

The Frobenius norm of an $m \times n$ matrix $\mathbf{A}$ is defined as the square root of the sum of the absolute squares of its elements,

$$||\mathbf{A}|| = \sqrt{\sum_{i=1}^{m}\sum_{j=1}^{n}|a_{ij}|^2}. \tag{17}$$

In case of compressible magnetosonic turbulence in the inner heliosheath, we need to use Equation 16 rather than Equation 14 to calculate the enstrophy density spectra. Therefore, the enstrophy density spectra in Figure 4 were calculated from the square of the Frobenius norm of the velocity gradient. Using energy conservation and enstrophy conservation arguments in stationary conditions, Kraichnan (1967) predicted a double cascade scenario in 2-D turbulence. If the turbulence is forced at intermediate scales, an inverse energy cascade and a direct enstrophy cascade are expected to develop, where energy moves to large scales and enstrophy moves to small scales. So the directions of the energy and enstrophy fluxes are opposite.

The nonstationary nature of the dispersive shock wave, that is, the occasional steepening of nonlinear waves into shocklets, provides a constant source of magnetosonic perturbations in the downstream region. Downstream propagating linear LFF waves are expected to drive ion-ion hybrid resonance at the wavelength where the frequency of the linear waves matches the ion-ion hybrid resonance frequency (see Figure 1a). The ion-ion hybrid resonance instability forces nonlinear magnetosonic waves at this intermediate scale. Since the velocity perturbations of perpendicular fast magnetosonic waves are two-dimensional, Kraichnan's theory (Kraichnan, 1967) predicts an inverse cascade of kinetic energy at large scales and a forward cascade of enstrophy at small scales in these downstream propagating waves. Overturning magnetosonic waves eventually result in forward and reverse shocklets that launch downstream (and upstream) propagating linear magnetosonic waves again further and further downstream, and the development of the double cascade is repeated multiple times. This process is expected to create a fully developed stationary turbulent spectrum at wave numbers higher than the wave number of the overturning waves.

We are going to test and verify these theoretical predictions with numerical three-fluid simulation in section 3.

3. Simulation of Fast Magnetosonic Turbulence in the Inner Heliosheath

3.1. Overturning of Fast Magnetosonic Waves

As demonstrated in the paper by Zieger et al. (2015), the multifluid 1-D simulation of the TS produces remarkable agreement with Voyager 2 observations, reproducing not only the microstructure of the TS3 crossing but also the energy partitioning among thermal ions, PUIs, and electrons across the shock. In order to simulate the theoretically predicted overturning of downstream propagating fast magnetosonic waves in the inner heliosheath, we extended the grid of the 1-D simulation to 8 AU both upstream and downstream of the TS. We used the same upstream solar wind conditions as in the best fitting hot electron case in Zieger et al. (2015; $u_{SW,1}$ = 320.7 km/s, $n_{SW,1}$ = 0.001278 cm^{-3}, $T_{SW,1}$ = 4155 K, B_1 = 0.06703 nT,

21699402, 2020, 10, Downloaded from https://agupubs.onlinelibrary.wiley.com/doi/10.1029/2020JA028393 by Test, Wiley Online Library on [04/01/2023]. See the Terms and Conditions (https://onlinelibrary.wiley.com/terms-and-conditions) on Wiley Online Library for rules of use; OA articles are governed by the applicable Creative Commons License

$n_{PUI,1} = 0.0003195$ cm^{-3}, $T_{PUI,1} = 13.42$ MK, $p_{e,1} = 0.01833$ pPa) for TS3 and the same grid resolution of 1,000 km resolving the ion inertial length (4,700 km) in the inner heliosheath. It was shown that the numerical solution was practically the same with a grid resolution of 500 km, which means that grid convergence had been achieved.

The initial left and right states are given by the upstream and downstream plasma parameters of the TS, where the downstream parameters are calculated from the generalized Rankine-Hugoniot jump conditions for the total fluid (the mixture of cold thermal ions, hot PUIs, and electrons). These boundary conditions result in a standing quasi-stationary shock solution in the inertial frame. The simulation was run for 20 days physical time to study the long-term behavior of the upstream propagating dispersive shock wave and the nonlinear growth and overturning of the downstream propagating LFF and HFF waves. We stopped the simulation before the fastest wave (HFF mode) had reached the outflow boundary at 8 AU downstream of the TS to avoid artificial reflection of waves from the boundary. A snapshot of the magnetic field variations at and beyond the TS up to 2.2 AU downstream is shown in Figure 2a after 20 days of simulation in physical time. We show simulation results up to 2.2 AU because this is the distance that a solar wind parcel covers in 20 days in the inner heliosheath after crossing the TS. Although the different kinds of waves propagate much further downstream in the same time, the background solar wind parameters beyond 2.2 AU are not exact solutions of the three-fluid model but they represent only the initial downstream conditions of the simulation. For this reason, we limited our analysis to the downstream region up to 2.2 AU.

Our three-fluid simulation shows that the dispersive effects of fast magnetosonic waves are manifested on the scale of astronomical units (AU), and dispersion plays a key role in the generation of compressible turbulence in the inner heliosheath. The quasi-stationary trailing wave train of the TS does not extend to infinity. Downstream propagating positive dispersive HFF waves grow until they steepen into shocklets and eventually overturn starting to propagate backward in the frame moving downstream at the sound speed of the PUIs. Similarly, downstream propagating positive dispersive LFF waves (in the high wave number range of 0.005 to 0.05 ω_{pe}) grow nonlinearly until they steepen into shocklets and overturn as well. The counterpropagating fast magnetosonic waves (both LFF and HFF) produce fast magnetosonic turbulence in the heliosheath and limit the downstream extension of the quasi-stationary negative dispersive shock wave. Thus, our model produces coherent compressional waves in the postshock region immediately downstream the TS (see Figure 2b). Further downstream, nonlinear compressible turbulence develops in the inner heliosheath (see Figure 2a) due to the nonlinear steepening and overturning of fast magnetosonic waves. The temporal evolution of turbulence eventually leads to large-scale quasi-stationary structures like magnetic holes (see Figure 2c), and the turbulent kinetic energy is dissipated on large scales through solar wind heating and acceleration.

The negative dispersive shock wave in the magnetic field intensity shown in Figure 2b is produced by upstream propagating negative dispersive nonlinear LFF mode waves. The overshoot at the shock front is the soliton edge predicted by the theory of dispersive shock waves (Biskamp, 1973). The smallest amplitude waves at 0.1 AU represent the linear wave edge of the negative dispersive shock wave, which moves downstream in time in the shock frame as predicted by theory (Hoefer, 2014). The oscillatory nonlinear waves appear quasi-stationary in the shock frame because the phase velocity of the wave is the same as the downstream flow velocity of the solar wind plasma. This has been verified by measuring the wavelength and phase velocity of the dispersive shock wave in the simulation. The blue square symbol in Figure 1b marks the wave number and phase velocity obtained from the simulation. It lies exactly on the theoretical curve of the phase velocity of the LFF mode (blue line), implying a remarkable agreement between theory and the numerical three-fluid simulation. The nonlinear waves close to the soliton edge are nonsinusoidal and quasi-stationary in the sense that they can occasionally steepen into shocklets. The nonstationary nature of the dispersive shock wave provides a source of compressible disturbance that drives turbulence further downstream in the inner heliosheath.

The theoretically predicted expansion of the oscillatory region downstream of the TS has been confirmed by our 1-D three-fluid simulation. The linear wave edge of the negative dispersive shock wave reached 0.1 AU downstream of the TS in 66 hr. However, the linear wave edge eventually stopped moving downstream in the simulation. The dispersive shock wave became quasi-stationary in the shock frame after 82 hr and remained so until the end of the simulation at 22 days. This long-term behavior of the dispersive shock wave is probably

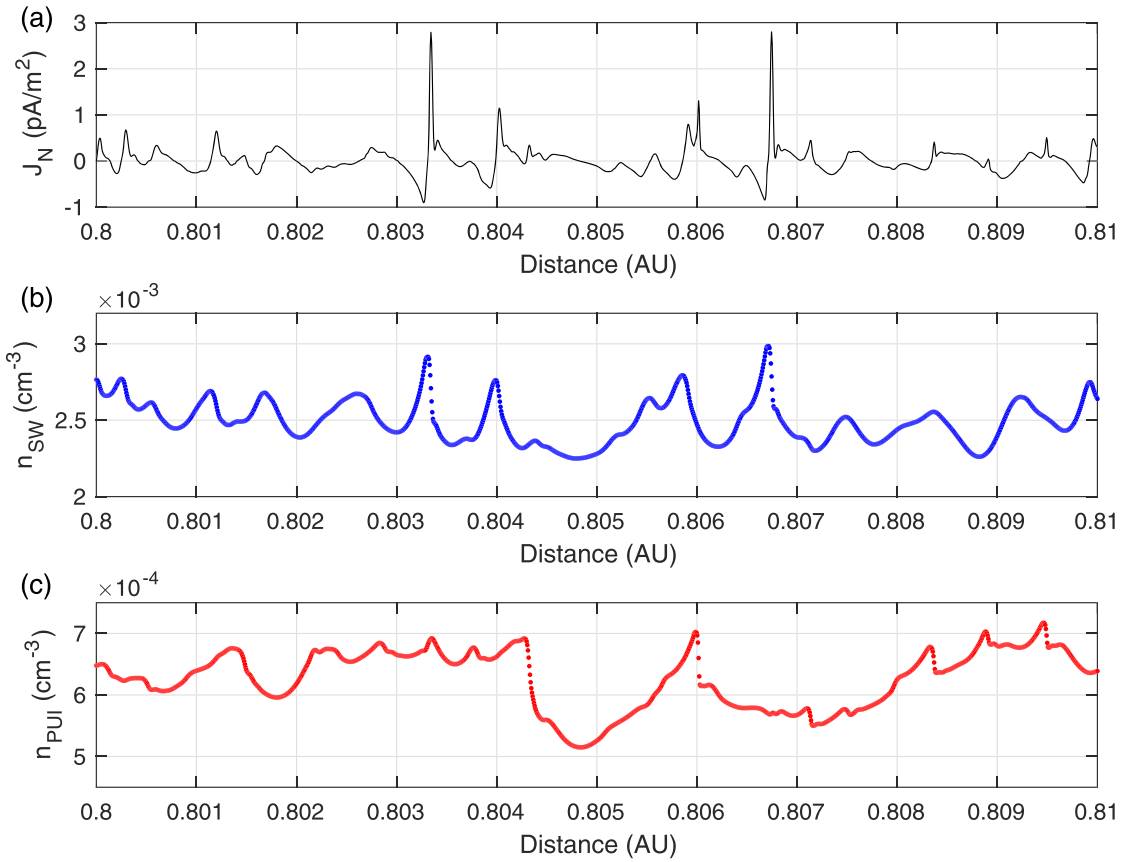

Figure 3. Nonlinear steepening of fast magnetosonic waves propagating downstream of the TS. (a) Thin current sheets associated with (b) forward shocklets in the solar wind ions (LFF mode) or (c) forward shocklets in the pickup ions (HFF mode). Since the two wave modes are independent, the occurrence of shocklets (sudden jumps or steep gradients in density) is not simultaneous in the solar wind ions and the pickup ions.

due to the change in the sign of the dispersion of the LFF mode at higher wave numbers ($ck > 0.005\ \omega_{pe}$), as shown in Figure 1c.

Our three-fluid MHD simulation confirms the theoretically predicted nonlinear steepening and overturning of downstream propagating perpendicular magnetosonic waves. The downstream propagating coherent LFF and HFF waves steepen into shocklets and start to propagate backward in the frame that propagates at the sound speed of the thermal solar wind ions or at the sound speed of the PUIs, respectively, which results in compressional turbulence further down in the inner heliosheath (see Figures 2a and 2c). The overturning distance depends on the growth rate of the downstream propagating positive dispersive nonlinear HFF and LFF modes. In this particular simulation, the downstream propagating nonlinear waves started to steepen into shocklets at around 0.8 AU downstream of the TS as shown in Figure 3. Since the LFF and HFF modes are independent, shocklets (sudden jumps) in the solar wind ion density (Figure 3b) and in the PUI density (Figure 3c) do not form simultaneously. However, both types of shocklets (LFF-mode and HFF-mode) appear as jumps in the magnetic field or peaks in the normal component of the current density (J_N), as shown in Figure 3a. Although all the shocklets in Figure 3 are forward shocklets, both forward and reverse shocklets occur further downstream in the turbulent inner heliosheath due to the overturning and counterpropagating fast magnetosonic waves.

As the turbulence develops in time in a downstream propagating fluid parcel, magnetic depressions or magnetic holes start to appear (see Figure 2c). The physical process leading to the formation of these magnetic structures deserves more thorough theoretical discussion that is outside the scope of this paper. Nevertheless, one can easily find out which wave mode is responsible for these magnetic holes that have been observed by both Voyager 1 (Burlaga et al., 2007) and Voyager 2 (Burlaga et al., 2016). We can follow the same procedure that we used to identify the wave mode of the trailing wave train downstream of the TS crossing. Using

21699402, 2020, 10, Downloaded from https://agupubs.onlinelibrary.wiley.com/doi/10.1029/2020JA028393 by Test, Wiley Online Library on [04/01/2023]. See the Terms and Conditions (https://onlinelibrary.wiley.com/terms-and-conditions) on Wiley Online Library for rules of use; OA articles are governed by the applicable Creative Commons License

21699402, 2020, 10, Downloaded from https://agupubs.onlinelibrary.wiley.com/doi/10.1029/2020JA028393 by Test, Wiley Online Library on [04/01/2023]. See the Terms and Conditions (https://onlinelibrary.wiley.com/terms-and-conditions) on Wiley Online Library for rules of use; OA articles are governed by the applicable Creative Commons License

two nearby time frames in the simulation, the propagation velocity of magnetic holes can be derived in the solar wind plasma frame by calculating a simple cross-correlation function. Furthermore, we can also calculate the average wavelength of magnetic holes. We found that these magnetic holes are not frozen in the solar wind but are propagating at a very low speed (−15.7 km/s) in the upstream direction in the plasma frame. Since the solar wind speed (181.9 km/s at 2 AU downstream of the TS) is much higher than the propagation speed of magnetic holes, the magnetic holes are propagating downstream in the inertial frame. The velocity and wave number of magnetic holes in the simulation defines a point (red square) in the group velocity plot of fast magnetosonic waves in Figure 1c that lies exactly on the group velocity curve of the HFF mode. This implies that magnetic holes are most probably produced by HFF waves that propagate upstream at frequencies close to the ion-ion hybrid resonance frequency.

3.2. Double Cascade of Energy and Enstrophy

In order to study the temporal evolution of turbulence in a downstream propagating solar wind plasma parcel, we calculated the power spectra of different solar wind variables at increasing distances from the TS. Since downstream propagating fast magnetosonic waves are continuously generated by the TS, which is a quasi-stationary dispersive shock wave, a solar wind plasma element is exposed to magnetosonic perturbations the longer time, the further it has been carried downstream of the shock. Thus, the turbulence becomes more and more developed as we move further away from the TS.

First, we consider the spectral evolution of downstream propagating nonlinear fast magnetosonic waves before they overturn due to nonlinear steepening. As it is shown in Figure 2a, the amplitude of coherent fast magnetosonic waves is gradually increasing between 0.2 and 0.8 AU until a maximum amplitude is reached around 0.8 AU. This is the point where downstream propagating LFF and HFF waves steepen into shocklets (see Figure 3), overturn, and start to propagate backward in the frame of the downstream propagating wave, which eventually leads to turbulence further downstream.

The evolution of the turbulent kinetic energy density spectra of solar wind ions and PUIs between 0.2 and 0.8 AU is shown in Figures 4a and 4b, respectively. Similarly, the evolution of the enstrophy density spectra of solar wind ions and PUIs is shown in Figures 4c and 4d. The power spectra were calculated in a 0.4 AU sliding window with 0.2 AU stepping, which gives 50% data overlap between adjacent spectra. Each spectrum was produced with Welchs-averaged periodogram method as follows. The 0.4 AU segment was divided into several smaller segments with 50% overlap. A modified periodogram was computed for each segment using a Hamming window, and all the resulting Fourier spectra were averaged to compute the final power spectral density (PSD) estimate. This averaging method is to reduce the noise in the high-frequency part of the spectra.

The turbulent kinetic energy of solar wind ions and PUIs develop an inverse energy cascade in time where the energy moves toward large scales. This can be seen as a shift of spectral power toward larger and larger scales as the solar wind moves downstream from 0.2 to 0.8 AU. The arrows in Figures 4a and 4b indicate the direction of the energy flux. On the other hand, the enstrophy of solar wind ions and PUIs develops a direct energy cascade in time, where enstrophy moves toward small scales. This is shown by the shift of spectral power to smaller and smaller scales as the solar wind moves downstream from 0.2 to 0.8 AU. The arrows in Figures 4c and 4d indicate the direction of the enstrophy flux. This is consistent with the double cascade scenario in 2-D turbulence with steady forcing. The vertical dashed lines indicate the theoretically predicted wave number of ion-ion hybrid resonance instability of solar wind ions and PUIs, which divides the inverse and forward cascade ranges. This implies that the 2-D magnetosonic turbulence is forced by the ion-ion hybrid resonance instability. At 0.2 AU, the enstrophy density of solar wind ions has a large narrow peak at the wave number of the ion-ion hybrid resonance instability and other smaller peaks at its harmonics (see Figure 4c), which confirms that the source of enstrophy is indeed the ion-ion hybrid resonance, where solar wind ions and PUIs collectively gyrate around each other. As the waves propagate downstream, enstrophy gradually moves to smaller scales. The turbulent kinetic energy of solar wind ions also has a strong initial peak at the wave number of the ion-ion hybrid resonance instability at 0.2 AU (see Figure 4a). The highest narrow peak is produced not by downstream propagating waves but by the upstream propagating dispersive shock wave because the first 0.4 AU segment includes the TS as well. As the kinetic energy spectrum of downstream propagating waves evolve in time, energy gradually moves to larger scales until a quasi-steady spectrum is formed at 0.8 AU distance from the TS. At this point, a maximum power is reached in kinetic

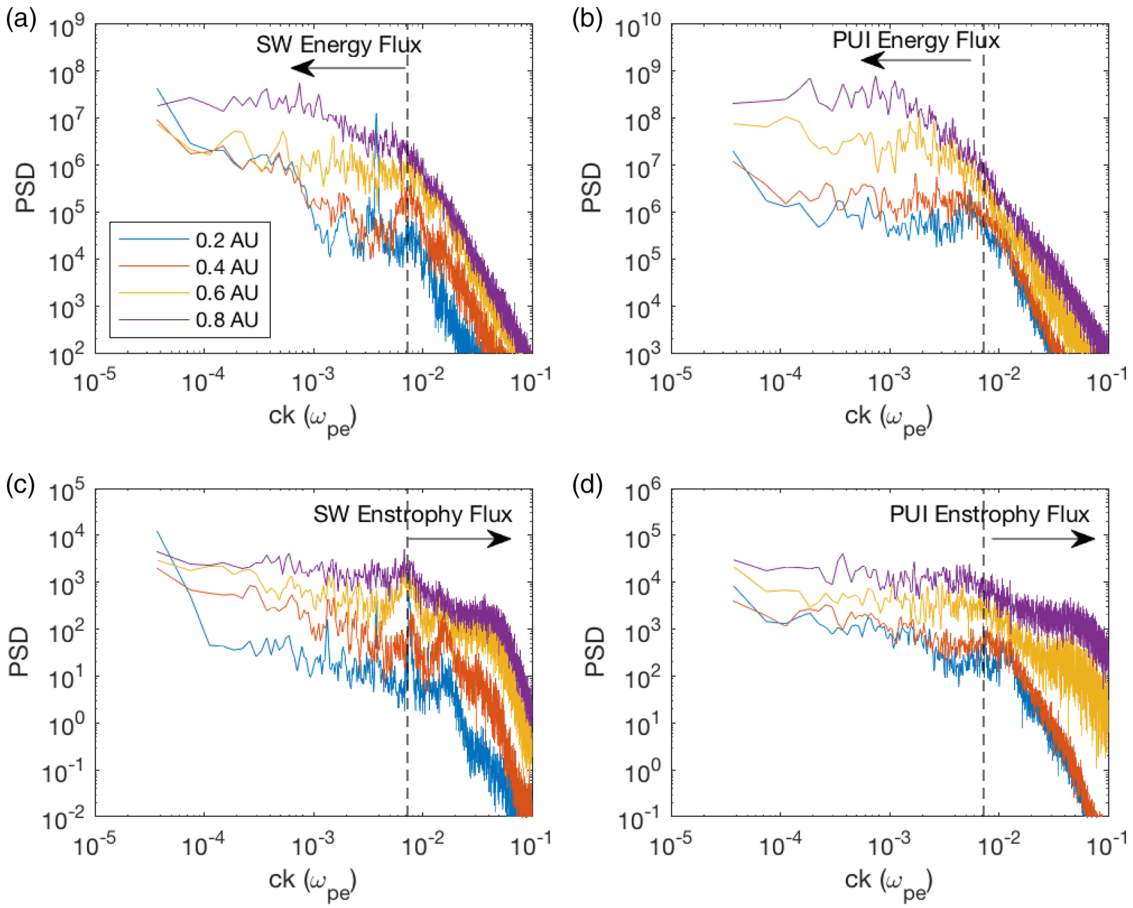

Figure 4. Inverse cascade of kinetic energy and direct cascade of enstrophy in fast magnetosonic waves propagating downstream in the plasma frame. (a) Kinetic energy density spectra of solar wind ions. (b) Kinetic energy density spectra of pickup ions. (c) Enstrophy density spectra of solar wind ions. (d) Enstrophy density spectra of pickup ions at different distances from the TS. Kinetic energy is transferred from small scales to large scales in the inverse cascade range, and enstrophy is transferred from large scales to small scales in the direct cascade range. The vertical dashed line in each panel is the theoretically predicted wave number of the ion-ion hybrid resonance in the LFF mode (see blue asterisk in Figure 1a).

energy at the wave number where the downstream propagating waves overturn. The power of downstream propagating waves cannot grow further because they steepen into shocklets at this scale.

The evolution of the energy and enstrophy spectra of PUIs (see Figures 4b and 4d) is very similar to that of the solar wind ions, showing a double cascade below and above the wave number of the ion-ion hybrid resonance instability. This means that not only the LFF mode but also the HFF mode is forced by the ion-ion hybrid resonance instability. A quasi-steady spectrum is formed at 0.8 AU in the PUI turbulent kinetic energy as well. However, the shapes of the energy spectra are different for thermal ions and PUIs, and the wave numbers of the maximum power are different, too. This is because the scales (wave numbers) where downstream propagating waves overturn are different for the LFF and HFF modes.

Next, we follow the evolution of the turbulent spectra of different solar wind variables in the turbulent region beyond 0.8 AU. Figure 5 shows the thermal energy spectra of solar wind ions, PUIs, and electrons as well as the magnetic energy spectrum at different distances from the TS. Overturning magnetosonic waves start to propagate in the opposite direction, and the counterpropagating waves produce forward and reverse shocklets resulting in compressible fast magnetosonic turbulence. The randomly occurring reverse shocklets launch downstream propagating fast magnetosonic waves now and again, maintaining a quasi-stationary energy and enstrophy flux at ion scales. As a result, a quasi-stationary turbulent spectrum develops in the inner heliosheath at large distances from the TS. Shocklets launch not only downstream propagating waves but also upstream propagating waves in the plasma frame. Upstream propagating magnetosonic waves contribute to the inverse energy cascade on fluid scales predicted by Kraichnans theory of 2-D turbulence. There is a constant flux of thermal energy toward large scales as indicated by arrows in Figure 5. We verified

21699402, 2020, 10, Downloaded from https://agupubs.onlinelibrary.wiley.com/doi/10.1029/2020JA028393 by Test, Wiley Online Library on [04/01/2023]. See the Terms and Conditions (https://onlinelibrary.wiley.com/terms-and-conditions) on Wiley Online Library for rules of use; OA articles are governed by the applicable Creative Commons License

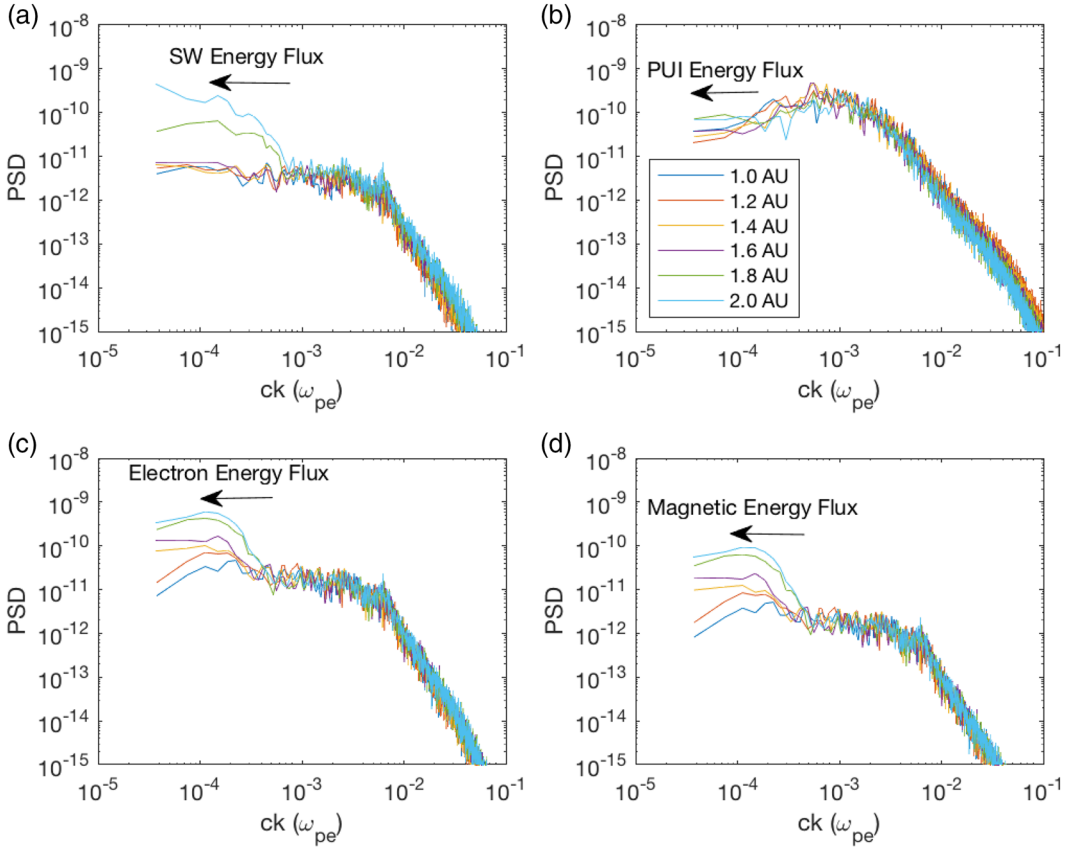

Figure 5. Inverse cascade of thermal energy in fast magnetosonic waves propagating upstream in the plasma frame. (a) Thermal energy density of solar wind ions. (b) Thermal energy density of pickup ions. (c) Thermal energy density of electrons. (d) Magnetic energy density at different distances from the TS. Thermal energy is transferred from small scales to large scales in the inner heliosheath.

that large-scale perturbations in the magnetic field, like magnetic holes in Figure 2c, and the associated large-scale perturbations in density, pressure, and thermal energy propagate upstream in the plasma frame at the group velocity of the HFF mode (see Figure 1c). This implies that the inverse energy cascade on fluid scale is mediated by upstream propagating HFF waves. The HFF mode approaches the frequency of the ion-ion hybrid resonance at large scales, which makes this wave mode unstable at the long wavelength limit. Since the group velocity of the HFF mode approaches zero at the long wavelength limit, the turbulent kinetic energy eventually dissipates on large scales in the form of solar wind heating and acceleration. The three-fluid simulation confirms the heating and acceleration of plasma as the turbulence develops in the downstream propagating solar wind. However, the discussion of solar wind heating and acceleration on the scales of astronomical units is outside the scope of this study.

3.3. Energy Spectra of Fully Developed Turbulence

We investigate the spectral properties of fully developed turbulence in our three-fluid simulation between 1.8 and 2.2 AU downstream of the TS. The magnetic field variations in this region are shown in Figure 2c. The goal of this analysis is to understand the spectral shapes of different turbulent variables, like velocity, density, pressure, energy, and magnetic field. Why are they different or why are they similar? Where do spectral breaks occur and what is their physical explanation? What can we learn about fast magnetosonic turbulence in the heliosheath if only magnetic observations were available?

The hydrodynamic energy spectra of solar wind ions and PUIs are shown in Figures 6a and 6b, respectively. The spectral slopes are significantly different, and the shape of the spectra is very different as well. This is attributed to the differences in the dispersion relations of the two fast magnetosonic modes. The spectral break in the hydrodynamic energy spectrum of solar wind ions in Figure 6a is at higher wave number ($\sim 4.7 \times 10^{-3}\ \omega_{pe}$) than the corresponding spectral break in the hydrodynamic energy spectrum of PUIs in

21699402, 2020, 10, Downloaded from https://agupubs.onlinelibrary.wiley.com/doi/10.1029/2020JA028393 by Test, Wiley Online Library on [04/01/2023]. See the Terms and Conditions (https://onlinelibrary.wiley.com/terms-and-conditions) on Wiley Online Library for rules of use; OA articles are governed by the applicable Creative Commons License

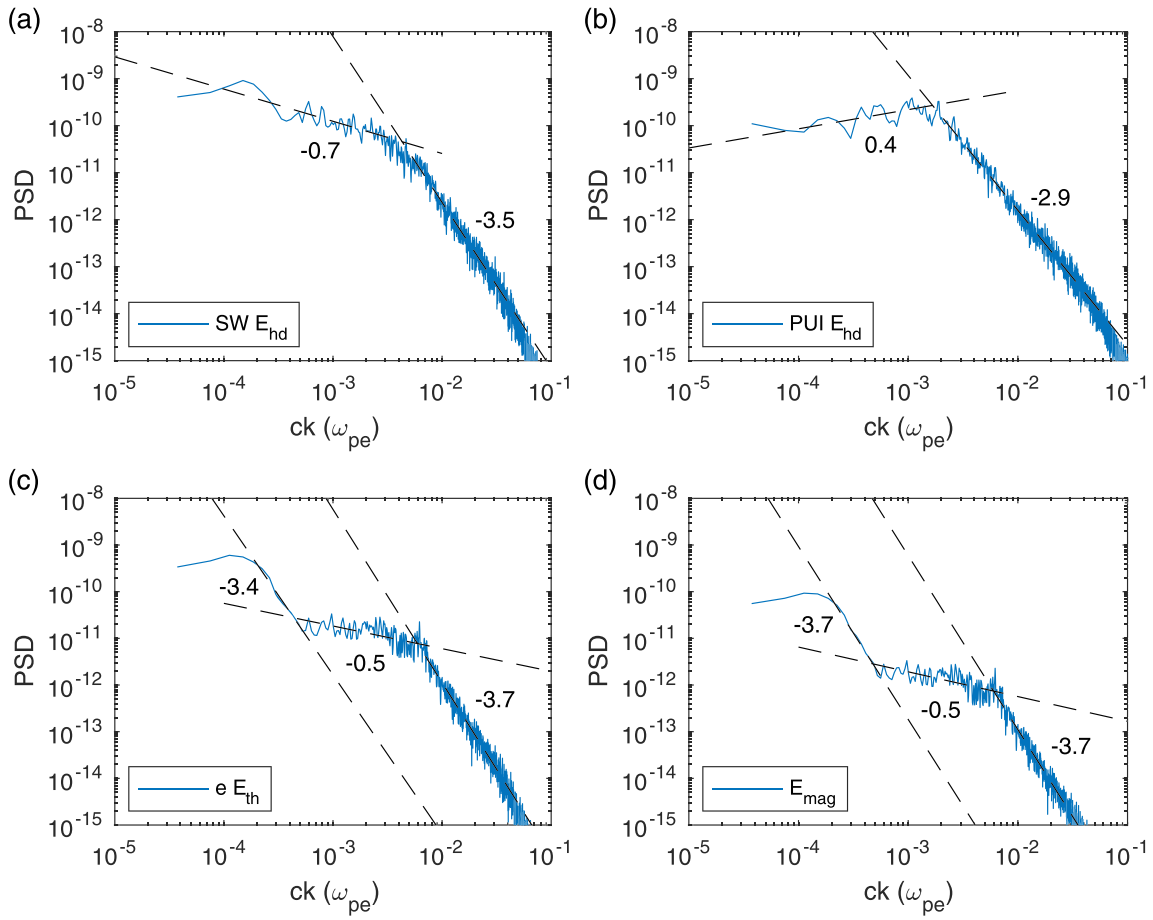

Figure 6. Energy spectra of fully developed magnetosonic turbulence in the inner heliosheath between 1.8 and 2.2 AU downstream of the TS. (a) Hydrodynamic energy spectrum of solar wind ions. (b) Hydrodynamic energy spectrum of pickup ions. (c) Thermal energy spectrum of electrons. (d) Magnetic energy spectrum. The best fitting spectral slopes are plotted as dashed lines and marked with the corresponding scaling exponents.

Figure 6b ($\sim 1.8 \times 10^{-3}\ \omega_{pe}$). These spectral breaks appear at the wave number where the downstream propagating nonlinear LFF and HFF waves steepen into shocklets and overturn. This is where the downstream propagating LFF and HFF waves reach their large-scale dissipation range above the intermediate-scale production range where the turbulence is forced by the ion-ion hybrid resonance instability (at the wave number of $7.3 \times 10^{-3}\ \omega_{pe}$).

The spectral break in the hydrodynamic energy spectrum of solar wind ions coincides with the wave number where the group velocity of LFF waves has a local minimum (see Figure 1c), that is, where $\mathrm{d}^2\omega_{SW}/\mathrm{d}k^2$ changes sign. LFF waves above the spectral break are positive dispersive and propagate downstream, while LFF waves below the spectral break are negative dispersive and propagate upstream in the frame of the downstream propagating wave. The spectral break in the hydrodynamic energy spectrum of PUIs coincides with the wave number where the second derivative of the group velocity of HFF waves has a local minimum, that is, where $\mathrm{d}^4\omega_{PUI}/\mathrm{d}k^4$) changes sign. Thus, the dissipation scales of LFF and HFF waves in inviscid collisionless plasma are determined by the shape of their dispersion relation not by the parameters of viscosity and large-scale friction, as in 2-D incompressible fluid turbulence (Kraichnan, 1967). Dissipation downstream of subcritical collisionless shocks is controlled by dispersion.

The scaling exponents of the hydrodynamic energy spectra in the production range where the turbulence is forced are −3.5 and −2.9 for solar wind ions and PUIs, respectively. In the range where the LFF and HFF waves overturn and propagate in the opposite direction, the scaling exponents of the hydrodynamic energy spectra are −0.7 for thermal ions and 0.4 for PUIs. The opposite spectral slopes can be explained with the sign of dispersion of overturning LFF and HFF waves. Overturning LFF waves become negative dispersive, while overturning HFF waves remain positive dispersive. Thus, upstream propagating LFF waves are amplified

21699402, 2020, 10, Downloaded from https://agupubs.onlinelibrary.wiley.com/doi/10.1029/2020JA028393 by Test, Wiley Online Library on [04/01/2023]. See the Terms and Conditions (https://onlinelibrary.wiley.com/terms-and-conditions) on Wiley Online Library for rules of use; OA articles are governed by the applicable Creative Commons License

and upstream propagating HFF waves are damped. However, damped HFF waves can still propagate because of the constant energy flux of the inverse cascade.

The hydrodynamic energy spectrum of electrons is practically identical with the thermal energy spectrum of electrons (Figure 6c) because of the negligible kinetic energy of electrons due to the low electron mass. It is very similar to the magnetic energy spectrum in Figure 6d. This similarity is not unexpected as in the multifluid model the magnetic field is frozen in the electron fluid (see Equation 4). For the same reason, the power spectrum of the electron density (or the total ion density) and the power spectrum of the magnetic field are expected to be very similar, too. Unlike in case of the hydrodynamic energy spectra of ions, the spectral break in the magnetic and electron energy spectra at intermediate scales coincides with the wave number of the ion-ion hybrid resonance instability ($7.3 \times 10^{-3}\ \omega_{pe}$). The second spectral break at the wave number of $\sim 4.5 \times 10^{-4}\ \omega_{pe}$ on fluid scale coincides with the wave number where the frequency of HFF waves approach the ion-ion hybrid resonance frequency, that is, $\omega_{PUI} \rightarrow \Omega_H$ (see Figure 1a). The inverse cascade of thermal energy (see Figure 5) and the inverse cascade of magnetic energy on fluid scales are therefore driven by HFF mode waves with frequencies approaching the proton gyrofrequency. The spectral slope of the inverse cascade on fluid scale is comparable to the spectral slope of the direct cascade on ion scale, both having a scaling exponent close to −3.7 (see Figures 6c and 6d). The inverse energy cascade on fluid scale is expected to extend to even larger scales as the turbulence develops in time, but our multifluid simulation was limited to 20 days physical time only. As demonstrated in Figure 6, the hydrodynamic energy spectra of thermal ions and PUIs are controlled by the dispersion of the LFF and HFF modes and do not reveal where the turbulence is forced. In contrast, the magnetic energy spectrum reveals the scale where the turbulence is forced but does not show the dissipation ranges of the HFF and LFF waves where the downstream propagating waves overturn.

In the next section, we are going to validate our three-fluid simulation of magnetosonic turbulence with high-resolution (48 s) magnetic field observation in the inner heliosheath by the Voyager 2 spacecraft.

4. Model Validation With Voyager 2 Observations

4.1. Reconstruction of the Voyager 2 TS Crossing

Voyager 2 crossed the TS multiple times on 31 August and 1 September 2007 at 83.7 AU from the Sun (Burlaga et al., 2008). The multiple crossings imply that the TS was not stationary but moved toward and away from the Sun due to varying upstream solar wind conditions. The compression ratios at the second (TS2) and third crossings (TS3) were in the range 2.1–2.4 and 1.6–1.8, respectively (Richardson et al., 2008; Zieger et al., 2015). Both TS2 and TS3 were subcritical perpendicular shocks with fast magnetosonic Mach numbers of 1.56 and 1.93, respectively. However, the upstream conditions at TS2 were more variable due to upstream solar wind turbulence. The microstructure of TS3 was successfully reconstructed by multifluid (Zieger et al., 2015) and particle-in-cell simulations (Yang et al., 2015). These simulations revealed a quasi-stationary shock structure with a ramp, an overshoot and an oscillatory wave train downstream of the shock front. The simulation of Yang et al. (2015) showed that the addition of 25% PUIs significantly reduced ion reflection from the shock. However, the shock front remained nonstationary exhibiting a rippled structure. Zieger et al. (2015) found that the multifluid simulation with 20% PUIs provided the best fit to Voyager 2 observations and concluded that the TS is a high-β low-Mach number subcritical dispersive shock wave. Voyager 2 observed strong compressible magnetic field variations in the 48 s magnetic data downstream the TS at the end of 2007 and in the beginning of 2008 (Burlaga & Ness, 2009). These compressible variations included large-amplitude coherent structures in the postshock region and weaker more random magnetic field variations in a unipolar region further downstream. The distribution of magnetic field increments was shown to be non-Gaussian on different scales from 48 s to several hours in both regions.

The large amplitude coherent magnetosonic waves observed in the post-shock region are consistent with the prediction of a coherent nonlinear dispersive shock wave downstream of the TS as shown in Figure 2b. Note that the upstream conditions were kept constant for 20 days in our simulation, which allowed the long-term temporal evolution of the dispersive shock wave. In reality, upstream conditions at the TS changed more rapidly, on the time scale of days or less, which limited the coherence length scale of dispersive shock waves. Consequently, the downstream region is expected to be a superposition of several dispersive shock waves with intermittent random variations.

21699402, 2020, 10, Downloaded from https://agupubs.onlinelibrary.wiley.com/doi/10.1029/2020JA028393 by Test, Wiley Online Library on [04/01/2023]. See the Terms and Conditions (https://onlinelibrary.wiley.com/terms-and-conditions) on Wiley Online Library for rules of use; OA articles are governed by the applicable Creative Commons License

4.2. Breaking Down of Taylor's Hypothesis

In order to allow direct comparison between the multifluid simulation and the high-resolution magnetic field observations of Voyager 2 in the inner heliosheath, we flew a virtual satellite in our time-dependent simulation across the turbulent downstream region at the speed of the Voyager 2 spacecraft and sampled the MHD variables in time domain. Then we calculated 48 s averages of the magnetic field and plasma variables to produce a simulated Voyager 2 time series that could be directly compared with actual data.

First, we wanted to test the validity of Taylor's hypothesis in the heliosheath, which assumes that the observed temporal variations in the spacecraft frame correspond to spatial variations in the plasma frame. This is generally thought to be valid in the supersonic solar wind due to the large velocity difference between the spacecraft and the solar wind but not necessarily valid in the heliosheath behind the TS where the fast magnetosonic speed exceeds the downstream flow velocity. The relationship between wave frequencies observed in the spacecraft frame (f_{SC}) and in the plasma frame (f_{PL}) can be described with the Doppler shift equation:

$$f_{SC} = f_{PL} + \frac{1}{2\pi}\mathbf{k}\cdot\mathbf{v}_{rel}, \tag{18}$$

where $\mathbf{k}$ is the wave number vector and $\mathbf{v}_{rel}$ is the relative velocity between the solar wind and the spacecraft. Taylor's hypothesis (Taylor, 1938) requires that

$$f_{PL} \ll \frac{1}{2\pi}\mathbf{k}\cdot\mathbf{v}_{rel}, \tag{19}$$

which means that the phase velocity of waves in the direction of the relative velocity is much smaller than the relative speed between the spacecraft and the solar wind ($v_{ph} = \omega/k \ll \mathbf{v}_{rel}$). Since the solar wind flow and the direction of motion of Voyager 2 is radially outward at the TS and the magnetic field is predominantly in the azimuthal direction, Taylor's hypothesis should be considered for the fastest wave mode in the perpendicular direction, which is the HFF mode. As shown in Figure 1b, the phase velocity of the perpendicular HFF mode is much larger than the downstream flow velocity of 182 km/s especially at large scales where the phase velocity exceeds 10^4 km/s. The phase velocity of the LFF mode is also larger than the downstream flow velocity (indicated by a blue square) on fluid scales, but it becomes smaller than that on ion and electron scales. Thus, Taylor's hypothesis clearly breaks down for fast magnetosonic turbulence.

In order to demonstrate the breaking down of Taylor's hypothesis in the inner heliosheath, we computed the turbulent spectra of solar wind ion density and PUI density both in wave number and frequency domains using the time series of the virtual spacecraft moving at the speed of Voyager 2 in the multifluid simulation. In Figure 7, we adjusted the frequency range to the wave number range with the linear conversion formula of Equation 18, assuming that Taylor's hypothesis was true. The spectra in wave number and frequency domains should be identical if Taylor's hypothesis was true. This is apparently not the case. The spectral shapes and the spectral slopes in Figure 7 are significantly different in the wave number and frequency domains both for solar wind ions and PUIs. This means that Taylor's hypothesis generally breaks down for both the LFF and HFF waves in the inner heliosheath. Although the density spectrum of solar wind ions looks like a Kolmogorov spectrum in frequency domain having a scaling exponent close to −5/3 on fluid scales, the actual scaling exponent is not −1.7 but −3.9 in wave number domain. This means that the turbulent spectrum of fast magnetosonic waves cannot be determined with a single spacecraft flying at the speed of Voyager 2. Only multispacecraft observations could distinguish between spatial and temporal variations in the inner heliosheath. Note that the spectral shape of solar wind ion density in Figure 7a and the spectral shapes of electron thermal energy and magnetic energy densities in Figures 6c and 6d are very similar. This can be understood as a consequence of the magnetic field being frozen in the electron fluid, the charge neutrality enforcing the total ion density to be the same as the electron density, and the dominance of solar wind ions over PUIs in the total ion density.

4.3. Comparison of Simulated and Observed Magnetic Field Turbulence

Since high-resolution magnetic data (48 s averages) are available from Voyager 2 in the inner heliosheath, we can directly compare the observed turbulent magnetic spectrum with the magnetic spectrum predicted by the three-fluid simulation in frequency domain at a virtual spacecraft flying at the speed of Voyager 2. For this purpose, we selected all the Voyager 2 data from 2009 when the spacecraft was sampling the fully developed turbulent region of the inner heliosheath. Since the typical length of continuous data segments is about 2 to

21699402, 2020, 10, Downloaded from https://agupubs.onlinelibrary.wiley.com/doi/10.1029/2020JA028393 by Test, Wiley Online Library on [04/01/2023]. See the Terms and Conditions (https://onlinelibrary.wiley.com/terms-and-conditions) on Wiley Online Library for rules of use; OA articles are governed by the applicable Creative Commons License

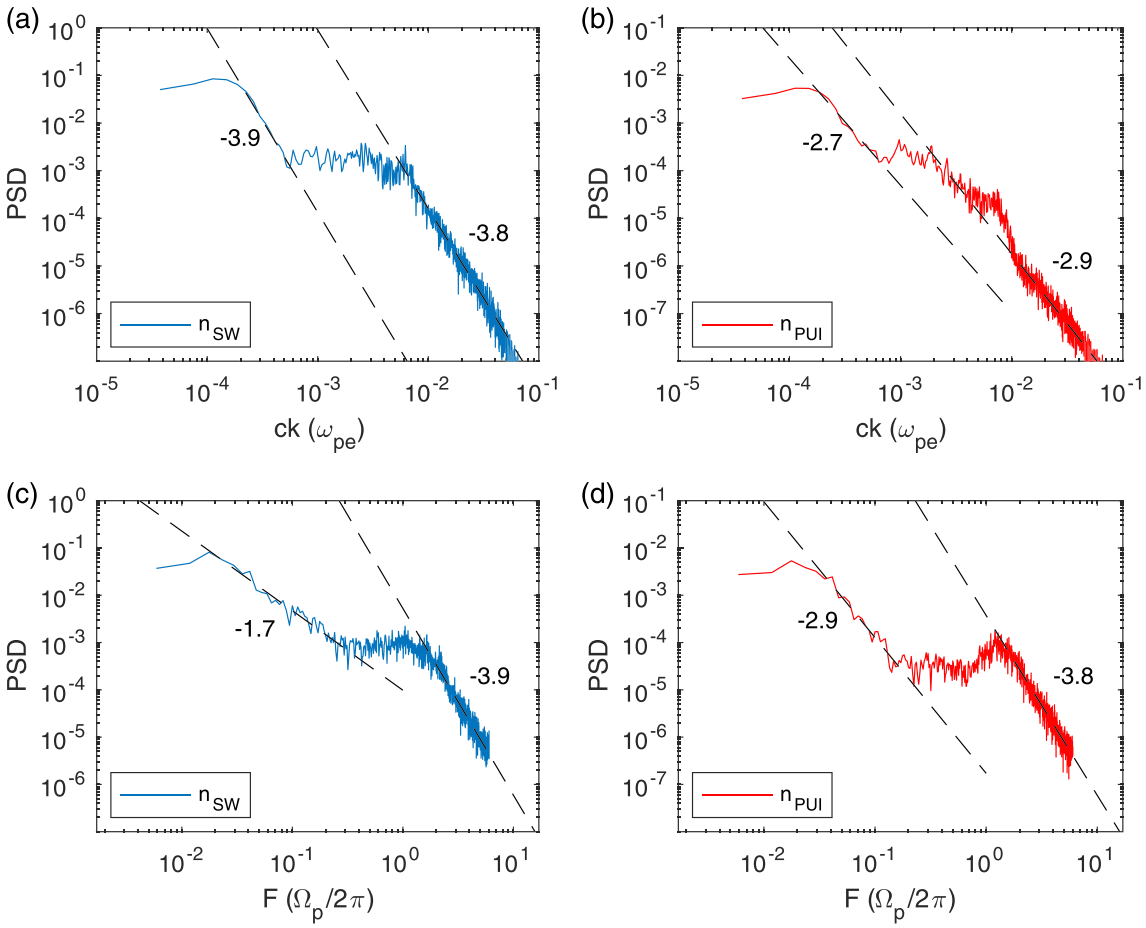

Figure 7. Breaking down of Taylor's hypothesis in the inner heliosheath. (a) Power spectrum of solar wind ion density in wave number domain. (b) Power spectrum of pickup ion density in wave number domain. (c) Power spectrum of solar wind ion density in frequency domain. (d) Power spectrum of pickup ion density in frequency domain as it would be observed by the Voyager 2 spacecraft between 1.8 and 2.2 AU downstream of the TS. The best fitting spectral slopes are plotted as dashed lines and marked with the corresponding scaling exponents. Since the density spectra are very different in the wave number and frequency domains for both solar wind ions and pickup ions, Taylor's hypothesis of observing predominantly spatial variations by a spacecraft in frequency domain apparently breaks down in the subfast magnetosonic inner heliosheath.

6 hr per day because of the telemetry constraints of Voyager 2, we limited our data analysis to the frequency range between 10^{-5} and 10^{-2} Hz to avoid artifacts at lower frequencies due to the long data gaps. Missing data were linearly interpolated to a regular grid of 48 s resolution. We applied Welshs averaged periodogram method described in section 3.2 to compute the average power spectrum of the turbulent magnetic field intensity observed by Voyager 2 in the year 2009. A similar spectrum was computed for the magnetic field time series of the virtual spacecraft flown in the multifluid simulation. The simulated and observed magnetic turbulence spectra are presented in Figures 8a and 8d.

The multifluid simulation closely reproduces the observed magnetic turbulence spectrum below the proton gyrofrequency with a scaling exponent of −1.7, which is very close to the Kolmogorov scaling exponent of −5/3 in incompressible fluids. However, as it is demonstrated in Figure 7, the spectral slope of magnetosonic turbulence in frequency domain is not the same as the spectral slope in wave number domain due to the breaking down of Taylor's hypothesis in the inner heliosheath. This implies that the observed turbulent magnetic field spectrum is not a classical forward-cascade Kolmogorov spectrum, contrary to Fraternale et al. (2019). The Voyager 2 turbulent magnetic spectrum (Figure 8c) also shows a narrow peak close to the proton gyrofrequency and its harmonics, which confirms the presence of ion-ion hybrid resonance. Resonance peaks at the gyrofrequencies of α particles and interstellar He^+ PUIs are also present, as predicted by theory. However, these minor ion species were not included in the numerical three-fluid simulation. The observed turbulent magnetic spectrum is known to be affected by noise at frequencies above the proton

21699402, 2020, 10, Downloaded from https://agupubs.onlinelibrary.wiley.com/doi/10.1029/2020JA028393 by Test, Wiley Online Library on [04/01/2023]. See the Terms and Conditions (https://onlinelibrary.wiley.com/terms-and-conditions) on Wiley Online Library for rules of use; OA articles are governed by the applicable Creative Commons License

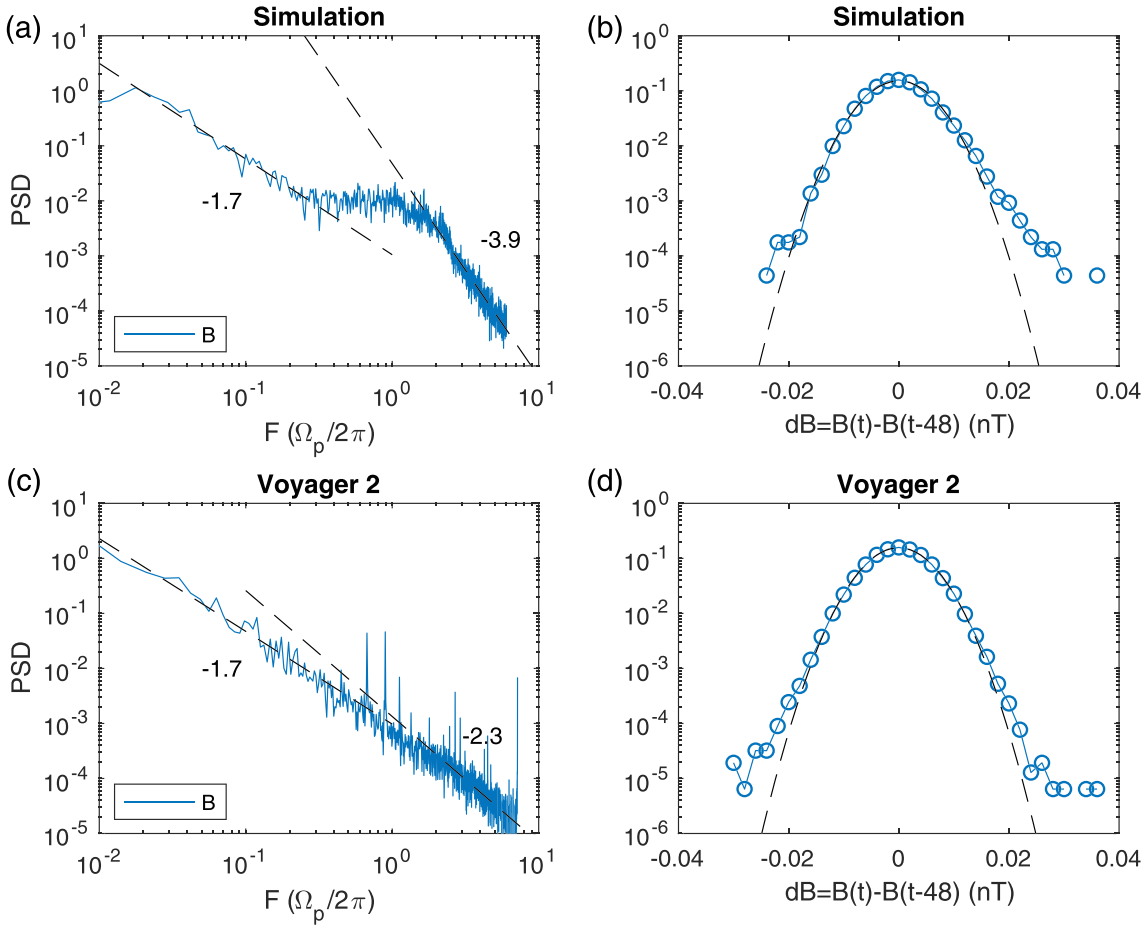

Figure 8. Model validation with Voyager 2 high-resolution magnetic field observations. (a) Simulated magnetic turbulence spectrum in frequency domain and (b) simulated distribution of magnetic field increments as it would be observed by the Voyager 2 spacecraft in the inner heliosheath. (c) Voyager 2 magnetic turbulence spectrum and (d) Voyager 2 distribution of magnetic field increments observed in the inner heliosheath in year 2009. The best fitting spectral slopes are plotted as dashed lines and marked with the corresponding scaling exponents in panels (a) and (c). The best fitting Gaussian distributions are plotted as dashed curves in panels (b) and (c). The three-fluid simulation closely reproduces the observed frequency-domain magnetic turbulence spectrum with a scaling exponent of −1.7 on fluid scale. The simulation also reproduces the observed non-Gaussian distribution of magnetic field increments in the inner heliosheath.

gyrofrequency (Fraternale et al., 2019). Therefore, we cannot make a reliable comparison between the simulated and observed turbulent magnetic spectra in the high-frequency dissipation range. Nevertheless, both the observed and simulated turbulent magnetic spectra exhibit a spectral break around the proton gyrofrequency, where the 2-D magnetosonic turbulence is forced by the ion-ion hybrid resonance instability.

Overturning downstream propagating LFF and HFF waves produce both forward and reverse shocklets in the fully developed turbulence region of the inner heliosheath. Shocklets appear as sudden jumps in the magnetic field, which is expected to produce outliers in the distribution of magnetic field increments. In order to validate the presence of forward and reverse shocklets in the turbulent inner heliosheath, we computed the distribution functions of magnetic field increments for the 48 s resolution Voyager 2 data. A similar distribution function was computed for the magnetic field time series of the virtual spacecraft in the multifluid simulation. The simulated and observed distribution functions of magnetic field increments are presented in Figures 8b and 8d. The best fitting Gaussian distributions are indicated by the dashed parabola curves. Both the observed and simulated distribution functions show significant deviations from Gaussian. The wings of the distributions at large positive and negative increments, which can be approximated with a symmetric Tsallis distribution at different scales (Burlaga & Ness, 2009), correspond to forward and reverse magnetosonic shocklets propagating downstream in the spacecraft frame. The similar shapes of the observed and simulated distribution functions confirm the presence of magnetosonic shocklets in the heliosheath and further validate the shock driven magnetosonic turbulence model.

21699402, 2020, 10, Downloaded from https://agupubs.onlinelibrary.wiley.com/doi/10.1029/2020JA028393 by Test, Wiley Online Library on [04/01/2023]. See the Terms and Conditions (https://onlinelibrary.wiley.com/terms-and-conditions) on Wiley Online Library for rules of use; OA articles are governed by the applicable Creative Commons License

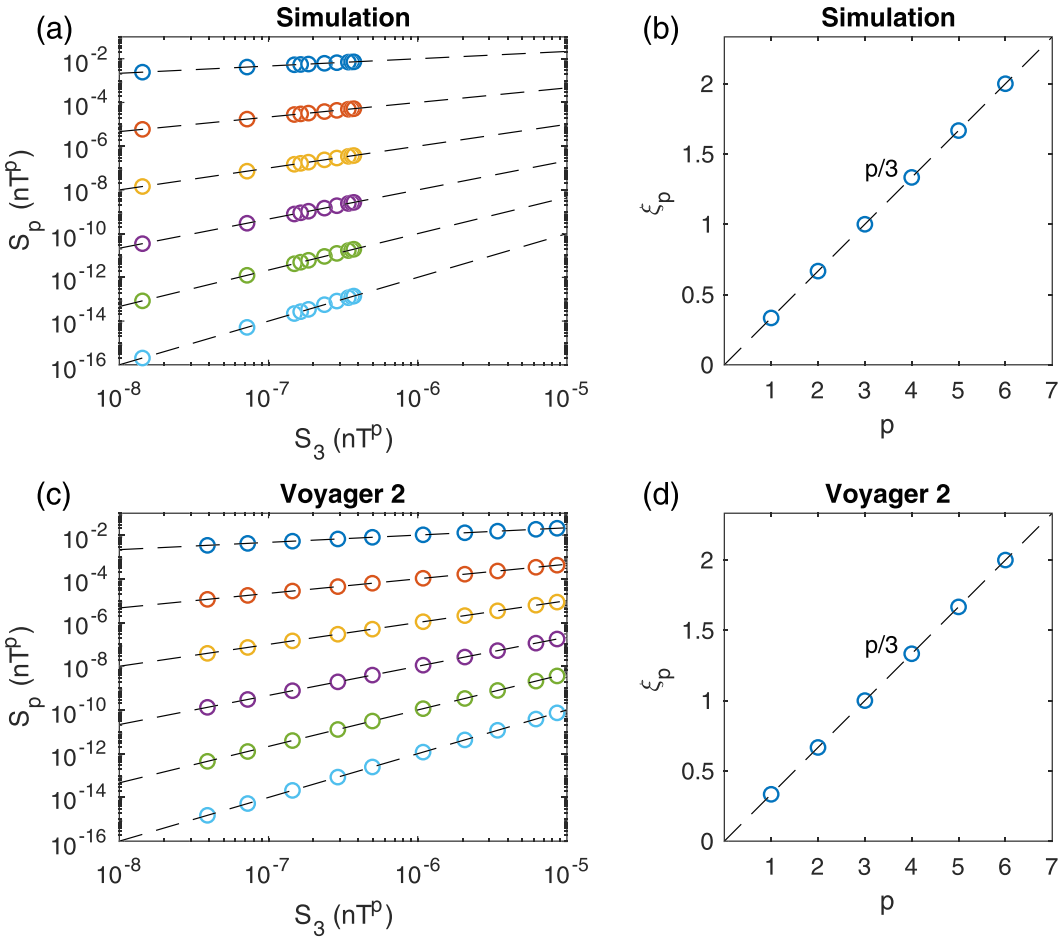

Figure 9. Kolmogorov-Kraichnan scaling of fast magnetosonic turbulence in the inner heliosheath. (a) Scaling of simulated magnetic field structure functions as a function of the third-order moment. (b) Scaling exponents of the structure functions in panel (a) as a function of the order p. (c) Scaling of Voyager 2 magnetic field structure functions observed in the inner heliosheath in year 2009 as a function of the third-order moment. (d) Scaling exponents of the structure functions in panel (c) as a function of the order p. The best linear fits are plotted as dashed lines in panels (a) and (c). The predicted $p/3$ scaling of the scaling exponents is plotted as dashed lines in panels (b) and (d). The three-fluid simulation reproduces the observed Kolmogorov-Kraichnan scaling of compressible turbulence in the inner heliosheath.

In order to analyze the multiscale properties of fast magnetosonic turbulence in the inner heliosheath, we computed the structure functions of the magnetic field for the simulated time series of the virtual spacecraft flown at the speed of Voyager 2 across the fully developed turbulence region of the multifluid simulation. As a comparison, we computed the magnetic structure functions at Voyager 2 in the inner heliosheath in year 2009. We used only the existing data points in this analysis without interpolating over the data gaps. The magnetic structure function is defined as

$$S_p(\tau) = \langle |B(t) - B(t+\tau)|^p \rangle, \tag{20}$$

where p is the order of the structure function, τ is the difference in time, and the angle brackets mean the expected value. The structure functions were evaluated up to the sixth order at the smallest scales with τ ranging from 48 s to 6 hr. At larger scales the Voyager 2 magnetic structure functions are strongly affected by the data gaps. Kraichnans theory of 2-D turbulence predicts that the structure functions do not scale close to the production range where the turbulence is forced. However, the structure functions should scale as a function of the third-order moment, and the scaling exponents should be $p/3$, which is referred to as Kolmogorov-Kraichnan scaling.

21699402, 2020, 10, Downloaded from https://agupubs.onlinelibrary.wiley.com/doi/10.1029/2020JA028393 by Test, Wiley Online Library on [04/01/2023]. See the Terms and Conditions (https://onlinelibrary.wiley.com/terms-and-conditions) on Wiley Online Library for rules of use; OA articles are governed by the applicable Creative Commons License

We plotted the magnetic structure functions as a function of the third-order moment in Figures 9a and 9c for the simulated and observed compressible turbulence, respectively. The structure functions perfectly scale as a function of the third-order moment. The dashed lines represent the best linear fits, and the slopes of the best fitting lines provide a scaling exponent (ξ_p) for each structure function. These scaling exponents are plotted as a function of p in Figures 9b and 9d for the simulated and observed turbulence, respectively. The scaling exponents of the structure functions (ξ_p) follow the theoretically predicted Kolmogorov-Kraichnan scaling, indicated as a dashed line in Figures 9b and 9d, with the scaling exponent of $p/3$ for both the simulated and observed compressible turbulence. The Kolmogorov-Kraichnan scaling is equivalent to the self-similarity of the turbulence at different scales. This can be proven as follows. The Kolmogorov-Kraichnan scaling states that

$$\log S_4 = \frac{4}{3}\log S_3 + c_1, \tag{21}$$

$$\log S_2 = \frac{2}{3}\log S_3 + c_2, \tag{22}$$

where c_1 and c_2 are constants. From Equations 21 and 22 we get

$$\log S_4 = 2\log S_2 + c_3, \tag{23}$$

where c_3 is constant. This means that S_4/S_2^2 is constant, which is the definition of self-similarity in turbulence theory. Thus, we have shown that the 2-D fast magnetosonic turbulence in the inner heliosheath is self-similar at different scales.

5. Conclusions

We have shown that the dispersion of fast magnetosonic waves in the nonequilibrium solar wind plasma plays an important role in the energy dissipation downstream of the TS. Due to the hot PUIs, the TS is a subcritical quasi-stationary dispersive shock wave consisting of a foot, a ramp, an overshoot, and an extended oscillatory region downstream of the shock front. The nonstationary nature of the dispersive shock wave provides a constant source of downstream propagating fast magnetosonic perturbations even in case of steady upstream solar wind conditions. Downstream propagating nonlinear fast magnetosonic waves grow until they reach a maximum amplitude and overturn, starting to propagate backward in the frame of the downstream propagating wave. The counterpropagating fast magnetosonic waves result in forward and reverse shocklets that maintain self-consistent quasi-stationary compressible turbulence in the inner heliosheath. The nonlinear growth of magnetosonic waves is driven by the ion-ion hybrid resonance instability of solar wind ions and PUIs. The 2-D compressible turbulence in the inner heliosheath shows a double cascade where energy is transferred to large scales and enstrophy is transferred to small scales as predicted by Kraichnans theory. The inverse energy cascade eventually heats and accelerates the solar wind plasma at the large wavelength limit. The numerical three-fluid simulation of the TS and the inner heliosheath has been validated with high-resolution magnetic field observations by Voyager 2. The magnetic turbulence spectrum observed by Voyager 2 is closely reproduced by the simulation in frequency domain below the proton gyrofrequency. However, it has been shown that Taylor's hypothesis breaks down in the inner heliosheath. Consequently, the observed magnetic turbulence spectrum is not a Kolmogorov spectrum in wave number domain. The observed non-Gaussian distribution of magnetic field increments has been explained with shocklets produced by nonlinearly steepened fast magnetosonic waves. Last but not the least, the multiscale analysis of magnetic field variations revealed a self-similar compressible turbulence on ion scales close to the production range where the turbulence is forced by ion-ion hybrid resonance in agreement with Kraichnans theory of 2-D turbulence and Voyager 2 observations in the inner heliosheath. In this study we simulated the TS in a one-dimensional domain with constant upstream solar wind conditions. Further work is needed to explore the nonstationary nature of the TS in two-dimensional geometry, with turbulent upstream solar wind driving and more realistic ion composition that includes solar He^{++} ions as well as interstellar He^{+} PUIs. These minor ion species are expected to introduce additional fast magnetosonic modes as well as additional ion-ion resonance peaks in the turbulent magnetic spectrum.

21699402, 2020, 10, Downloaded from https://agupubs.onlinelibrary.wiley.com/doi/10.1029/2020JA028393 by Test, Wiley Online Library on [04/01/2023]. See the Terms and Conditions (https://onlinelibrary.wiley.com/terms-and-conditions) on Wiley Online Library for rules of use; OA articles are governed by the applicable Creative Commons License

Data Availability Statement

The 48 s resolution Voyager 2 magnetic field data are accessible online (https://vgrmag.gsfc.nasa.gov/data.html).

Acknowledgments
B. Z. was mainly supported by NASA under Grant 80NSSC18K1214. The authors were partially supported by NASA DRIVE Grant 80NSSC20K0603, Our Heliospheric Shield. V. F. was partially supported by NASA Grant 80NSSC18K1209.

References

Balogh, A., & Treumann, R. A. (2013). *Physics of collisionless shocks*. New York: Springer. https://doi.org/10.1007/978-1-4614-6099-2
Biskamp, D. (1973). Collisionless shock waves in plasmas. *Nuclear Fusion*, *13*, 719–740. https://doi.org/10.1088/0029-5515/13/5/010
Burlaga, L. F., & Ness, N. F. (2009). Compressible "turbulence" observed in the heliosheath by Voyager 2. *Astrophysical Journal*, *703*(1), 311–324. https://doi.org/10.1088/0004-637X/703/1/311
Burlaga, L. F., Ness, N. F., Acuña, M. H., Lepping, R. P., Connerney, J. E. P., & Richardson, J. D. (2008). Magnetic fields at the solar wind termination shock. *Nature*, *454*(7200), 75–77. https://doi.org/10.1038/nature07029
Burlaga, L. F., Ness, N. F., & Acuna, M. H. (2007). Linear magnetic holes in a unipolar region of the heliosheath observed by Voyager 1. *Journal of Geophysical Research*, *112*, A07106. https://doi.org/10.1029/2007JA012292
Burlaga, L. F., Ness, N. F., Richardson, J. D., Decker, R. B., & Krimigis, S. M. (2016). Heliosheath magnetic field and plasma observed by Voyager 2 during 2012 in the rising phase of solar cycle 24. *Astrophysical Journal*, *818*(2), 147. https://doi.org/10.3847/0004-637X/818/2/147
Chalov, S. V., & Fahr, H. J. (2013). The role of solar wind electrons at the solar wind termination shock. *Monthly Notices of the Royal Astronomical Society*, *433*, L40–L43. https://doi.org/10.1093/mnrasl/slt052
Chashei, I. V., & Fahr, H. J. (2014). On solar-wind electron heating at large solar distances. *Solar Physics*, *289*(4), 1359–1370. https://doi.org/10.1007/s11207-013-0403-8
Coroniti, F. V. (1970). Dissipation discontinuities in hydromagnetic shock waves. *Journal of Plasma Physics*, *4*(2), 265–282. https://doi.org/10.1017/S0022377800004992
Dubinin, E. M., Sauer, K., & McKenzie, J. F. (2006). Nonlinear 1-D stationary flows in multi-ion plasmas-sonic and critical loci-solitary and "oscillatory" waves. *Annales Geophysicae*, *24*(11), 3041–3057. https://doi.org/10.5194/angeo-24-3041-2006
Edmiston, J. P., & Kennel, C. F. (1984). A parametric survey of the first critical Mach number for a fast MHD shock. *Journal of Plasma Physics*, *32*(3), 429–441. https://doi.org/10.1017/S002237780000218X
Fahr, H. J., Chashei, I. V., & Verscharen, D. (2014). Traveling solar-wind bulk-velocity fluctuations and their effects on electron heating in the heliosphere. *Astronomy & Astrophysics*, *571*, A78. https://doi.org/10.1051/0004-6361/201424421
Fahr, H.-J., Sylla, A., Fichtner, H., & Scherer, K. (2016). On the evolution of the κ distribution of protons in the inner heliosheath. *Journal of Geophysical Research: Space Physics*, *121*, 8203–8214. https://doi.org/10.1002/2016JA022561
Fraternale, F., Pogorelov, N. V., Richardson, J. D., & Tordella, D. (2019). Magnetic turbulence spectra and intermittency in the heliosheath and in the local interstellar medium. *Astrophysical Journal*, *872*(1), 40. https://doi.org/10.3847/1538-4357/aafd30
Glocer, A., Tóth, G., Ma, Y., Gombosi, T., Zhang, J. C., & Kistler, L. M. (2009). Multifluid block-adaptive-tree solar wind roe-type upwind scheme: Magnetospheric composition and dynamics during geomagnetic storms—Initial results. *Journal of Geophysical Research*, *114*, A12203. https://doi.org/10.1029/2009JA014418
Hoefer, M. A. (2014). Shock waves in dispersive Eulerian fluids. *Journal of Nonlinear Science*, *24*(3), 525–577. https://doi.org/10.1007/s00332-014-9199-4
Isenberg, P. A. (1986). Interaction of the solar wind with interstellar neutral hydrogen: Three-fluid model. *Journal of Geophysical Research*, *91*(A9), 9965–9972. https://doi.org/10.1029/JA091iA09p09965
Kraichnan, R. H. (1967). Inertial ranges in two-dimensional turbulence. *Physics of Fluids*, *10*(7), 1417–1423. https://doi.org/10.1063/1.1762301
McComas, D. J., Zirnstein, E. J., Bzowski, M., Elliott, H. A., Randol, B., Schwadron, N. A., et al. (2017). Interstellar pickup ion observations to 38 au. *Astrophysical Journal Supplement Series*, *233*(1), 8. https://doi.org/10.3847/1538-4365/aa91d2
McKenzie, J. F., Marsch, E., Baumgaertel, K., & Sauer, K. (1993). Wave and stability properties of multi-ion plasmas with applications to winds and flows. *Annales Geophysicae*, *11*(5), 341–353.
Opher, M., Loeb, A., Drake, J., & Toth, G. (2020). A small and round heliosphere suggested by magnetohydrodynamic modelling of pick-up ions. *Nature Astronomy*, *4*, 675–683. https://doi.org/10.1038/s41550-020-1036-0
Randol, B. M., McComas, D. J., & Schwadron, N. A. (2013). Interstellar Pick-up Ions Observed between 11 and 22 AU by New Horizons. *Astrophysical Journal*, *768*(2), 120. https://doi.org/10.1088/0004-637X/768/2/120
Richardson, J. D., Kasper, J. C., Wang, C., Belcher, J. W., & Lazarus, A. J. (2008). Cool heliosheath plasma and deceleration of the upstream solar wind at the termination shock. *Nature*, *454*(7200), 63–66. https://doi.org/10.1038/nature07024
Scherer, K., Fahr, H. J., Fichtner, H., Sylla, A., Richardson, J. D., & Lazar, M. (2018). Uncertainties in the heliosheath ion temperatures. *Annales Geophysicae*, *36*(1), 37–46. https://doi.org/10.5194/angeo-36-37-2018
Stone, E. C., Cummings, A. C., McDonald, F. B., Heikkila, B. C., Lal, N., & Webber, W. R. (2005). Voyager 1 explores the termination shock region and the heliosheath beyond. *Science*, *309*(5743), 2017–2020. https://doi.org/10.1126/science.1117684
Stone, E. C., Cummings, A. C., McDonald, F. B., Heikkila, B. C., Lal, N., & Webber, W. R. (2008). An asymmetric solar wind termination shock. *Nature*, *454*(7200), 71–74. https://doi.org/10.1038/nature07022
Taylor, G. I. (1938). The spectrum of turbulence. *Proceedings of the Royal Society*, *164*(919), 476–490. https://doi.org/10.1098/rspa.1938.0032
Toida, M., & Aota, Y. (2013). Finite beta effects on low- and high-frequency magnetosonic waves in a two-ion-species plasma. *Physics of Plasmas*, *20*(8), 82,301. https://doi.org/10.1063/1.4817169
Usmanov, A. V., & Goldstein, M. L. (2006). A three-dimensional MHD solar wind model with pickup protons. *Journal of Geophysical Research*, *111*, A07101. https://doi.org/10.1029/2005JA011533
Usmanov, A. V., Goldstein, M. L., & Matthaeus, W. H. (2014). Three-fluid, three-dimensional magnetohydrodynamic solar wind model with eddy viscosity and turbulent resistivity. *Astrophysical Journal*, *788*(1), 43. https://doi.org/10.1088/0004-637X/788/1/43
Whang, Y. C. (1998). Solar wind in the distant heliosphere. *Journal of Geophysical Research*, *103*(A8), 17,419–17,428. https://doi.org/10.1029/98JA01524
Yang, Z., Liu, Y. D., Richardson, J. D., Lu, Q., Huang, C., & Wang, R. (2015). Impact of pickup ions on the shock front nonstationarity and energy dissipation of the heliospheric termination shock: Two-dimensional full particle simulations and comparison with Voyager 2 observations. *Astrophysical Journal*, *809*(1), 28. https://doi.org/10.1088/0004-637X/809/1/28

21699402, 2020, 10, Downloaded from https://agupubs.onlinelibrary.wiley.com/doi/10.1029/2020JA028393 by Test, Wiley Online Library on [04/01/2023]. See the Terms and Conditions (https://onlinelibrary.wiley.com/terms-and-conditions) on Wiley Online Library for rules of use; OA articles are governed by the applicable Creative Commons License

Zank, G. P., Heerikhuisen, J., Pogorelov, N. V., Burrows, R., & McComas, D. (2010). Microstructure of the heliospheric termination shock: Implications for energetic neutral atom observations. *Astrophysical Journal*, *708*(2), 1092–1106. https://doi.org/10.1088/0004-637X/708/2/1092

Zank, G. P., Hunana, P., Mostafavi, P., & Goldstein, M. L. (2014). Pickup ion mediated plasmas. I. Basic model and linear waves in the solar wind and local interstellar medium. *Astrophysical Journal*, *797*(2), 87. https://doi.org/10.1088/0004-637X/797/2/87

Zieger, B., Opher, M., Schwadron, N. A., McComas, D. J., & Tóth, G. (2013). A slow bow shock ahead of the heliosphere. *Geophysical Research Letters*, *40*, 2923–2928. https://doi.org/10.1002/grl.50576

Zieger, B., Opher, M., Tóth, G., Decker, R. B., & Richardson, J. D. (2015). Constraining the pickup ion abundance and temperature through the multifluid reconstruction of the Voyager 2 termination shock crossing. *Journal of Geophysical Research: Space Physics*, *120*, 7130–7153. https://doi.org/10.1002/2015JA021437

21699402, 2020, 10, Downloaded from https://agupubs.onlinelibrary.wiley.com/doi/10.1029/2020JA028393 by Test, Wiley Online Library on [04/01/2023]. See the Terms and Conditions (https://onlinelibrary.wiley.com/terms-and-conditions) on Wiley Online Library for rules of use; OA articles are governed by the applicable Creative Commons License